



Formation of orange hibonite, as inferred from some Allende inclusions

S. B. SIMON^{1*}, A. M. DAVIS^{1,2} AND L. GROSSMAN^{1,2}

¹Department of the Geophysical Sciences, University of Chicago, 5734 South Ellis Avenue, Chicago, Illinois 60637, USA

²Enrico Fermi Institute, University of Chicago, 5640 South Ellis Avenue, Chicago, Illinois 60637, USA

*Correspondence author's e-mail address: sbs8@midway.uchicago.edu

(Received 2000 May 12; accepted in revised form 2000 November 22)

Abstract—We studied three fluffy Type A refractory inclusions from Allende that contain orange hibonite. The melilite in the present samples is very Al-rich, averaging Åk_6 , Åk_{14} , and Åk_{12} in the three samples studied. Hibonite in two inclusions, unlike that in Murchison, has low rare earth element abundances of $<10 \times \text{CI}$; in the other inclusion, the hibonite, melilite and perovskite have Group II-like patterns. The hibonite and melilite in all three inclusions studied have excess ^{26}Mg consistent with $(^{26}\text{Al}/^{27}\text{Al})_1 = 5 \times 10^{-5}$. Much of the hibonite and some of the spinel in these inclusions is corroded. These phases are found enclosed in melilite, but based on bulk compositions and phase equilibria, hibonite should not be an early-crystallizing phase in these inclusions. We conclude that the hibonite and probably some of the spinel is relic. Reversely zoned melilite, rounded spinel and isotopically heavy Mg in the inclusions probably reflect reheating events that involved melting and evaporation. Alteration of the gehlenitic melilite gave rise to some rare phases, including corundum and nearly pure CaTs pyroxene.

Studies have shown that blue hibonite contains Ti^{3+} while orange hibonite does not (Ihinger and Stolper, 1986; Beckett *et al.*, 1988). Orange hibonite formed either under oxidizing conditions (such as at oxygen fugacities at least seven orders of magnitude greater than that of a solar gas at 1700 K), or under conditions reducing enough (*e.g.*, solar) that it contained Ti^{3+} , which was later oxidized *in situ*. Although V and Ce oxides are volatile at the temperature and range of oxygen fugacities at which orange hibonite is known to be stable, we find that (a) the hibonite is V-rich ($\sim 1 \text{ wt\% V}_2\text{O}_3$) and (b) there are no negative Ce anomalies in Allende hibonite. This indicates that the hibonite did not form by condensation under oxidizing conditions. In addition, there are slight excesses of Ti + Si cations relative to Mg + Fe cations (up to 0.1 of 0.8 cations per 19 oxygen anions), probably reflecting the original presence of Ti^{3+} . The results of this study strongly support the suggestion (Ihinger and Stolper, 1986) that Allende hibonite originally formed under reducing conditions and was later oxidized. Oxygen fugacities within ~ 2 – 3 orders of magnitude of that of a solar gas are implied; otherwise, strong Ce and V depletions would be observed.

INTRODUCTION

Hibonite is important as a recorder of high-temperature processes in the early solar nebula. It is one of the first minerals to condense from a gas of solar composition at total pressures $<10^{-2}$ atm (Grossman, 1972; Yoneda and Grossman, 1995; Ebel and Grossman, 2000a); it can have a wide range of trace element abundances and chondrite-normalized rare earth element (REE) patterns, reflecting different histories (*e.g.*, Davis *et al.*, 1982; Ireland *et al.*, 1988, 1992); and it is commonly a carrier of large isotopic anomalies (*e.g.*, Ireland *et al.*, 1991; Simon *et al.*, 1998b), yielding important insights into the formation of the solar system. For these reasons, we need a good understanding of hibonite formation in all types of hibonite-

bearing inclusions. The refractory inclusion populations of CM2 chondrites, such as Murchison, are dominated by hibonite-bearing objects, but such inclusions are rare in CV3 chondrites, such as Allende. As a result, much is known about hibonite from Murchison, but very little about that in Allende, except for one feature: Ti-bearing hibonite in CM chondrites is blue, while that in Allende is generally tan or orange. This color difference has been shown to be related to the presence of Ti^{3+} in the blue hibonite and its absence in orange hibonite (Ihinger and Stolper, 1986). If the lack of Ti^{3+} in Allende hibonite is a primary feature, this would indicate that it formed under relatively oxidizing conditions that were not experienced by Murchison for any significant length of time. Alternatively, Allende hibonite could originally have formed under reducing

conditions, with oxidation of Ti^{3+} to Ti^{4+} occurring in a later, secondary process. This is the explanation preferred by Ihinger and Stolper (1986).

One way to determine which of these scenarios is correct is to measure the REE abundances in the Allende hibonite. If the hibonite condensed under oxidizing conditions, its chondrite-normalized REE patterns should exhibit negative Ce anomalies, because Ce^{4+} is more volatile than Ce^{3+} and the other trivalent REE (Davis *et al.*, 1982). Similarly, V becomes much less refractory under oxidizing conditions, such as in a CI gas, than it is in a solar gas (Davis *et al.*, 1982). These authors showed that strong Ce and V depletions relative to refractory elements are expected for condensates formed at oxygen fugacities five or six orders of magnitude greater than that of a solar gas (*i.e.*, approximately at the iron-wüstite buffer, or IW) at temperatures between 1450 and 1626 K (the latter is the appearance temperature of hibonite in their condensation calculation). Orange hibonite is not stable at oxygen fugacities below one order of magnitude greater than IW (henceforth IW+1) at 1700 K (Ihinger and Stolper, 1986). Therefore, hibonite that originally condensed under conditions sufficiently oxidizing to make it orange should have large negative V and Ce anomalies. In addition, Ti^{4+} and Mg enter hibonite together by substituting for two Al cations, whereas trivalent Ti can enter hibonite by direct substitution for Al. Thus, we can use the electron microprobe to determine if the Allende hibonite contains "excess" Ti relative to Mg, which would suggest that some of the Ti was originally trivalent and that the hibonite formed under solar, reducing conditions.

We studied three hibonite-bearing fluffy Type A (melilite-rich) refractory inclusions in Allende in an attempt to shed more light on the formation of hibonite in the early solar nebula. The present samples have many features in common with CG-11, a heavily altered, hibonite-rich Type A inclusion from Allende that was described in detail by Allen *et al.* (1978). They also exhibit some mineralogical and textural similarities to MUM-1 (MacPherson *et al.*, 1983), a rare, melilite-rich, hibonite-bearing inclusion from Murchison, and to CAI 3643, a complex hibonite-bearing inclusion from Allende (Wark, 1986). For this study, we analyzed hibonite by electron microprobe to determine its V contents and Ti-Mg systematics. We also used the ion microprobe to measure REE abundances in Allende hibonite, for comparison with hibonite from Murchison and to look for negative Ce anomalies. Preliminary results of this study were reported by Simon *et al.* (1998a).

ANALYTICAL METHODS

During an examination of Allende slab surfaces with a binocular microscope, we found three hibonite-rich inclusions, distinguished by the presence of a tan to light-orange phase. Polished thin sections were studied optically with a petrographic microscope. Backscattered electron images and x-ray maps were obtained and modal abundances of phases determined

with a JEOL JSM-5800 LV scanning electron microscope (SEM) equipped with an Oxford/Link ISIS-300 energy dispersive microanalysis system. Quantitative wavelength dispersive x-ray analyses were obtained with a Cameca SX-50 electron microprobe operated at 15 kV. Data were reduced *via* the modified ZAF correction procedure PAP (Pouchou and Pichoir, 1984).

Trace element and Mg isotopic analyses were obtained using the University of Chicago AEI IM-20 ion microprobe. The analytical techniques used are similar to those described in Simon *et al.* (1991), MacPherson and Davis (1993, 1994) and Russell *et al.* (2000). Trace element analyses were done using energy filtering. A variety of silicate standards were used to determine calcium-normalized ion yields. NIST 611 glass was analyzed at the beginning and end of each day to correct for day-to-day variations in ion yield that are a function of mass (MacPherson and Davis, 1994).

RESULTS

Petrography

ALH1, ALH2 and ALH3 (for Allende Hibonite) are melilite-rich, coarse-grained inclusions, and are best classified as fluffy Type A inclusions (MacPherson and Grossman, 1984). Sample ALH1 (Fig. 1a) is nodular and very irregular in shape, partially to completely enclosing sections of accretionary rim and pockets of the meteorite matrix in the plane of the thin section. This is the finest-grained and most heavily altered of the inclusions we studied. The outer edges of the nodules have Wark-Lovering rims (Wark and Lovering, 1977). Just inside the rims, the outer regions of the nodules, presumably originally melilite, are altered to anorthite + sodalite + grossular. The interiors of the nodules consist of hibonite \pm spinel enclosed in melilite. Melilite is mostly anhedral and 20–30 μm across. The spinel grains, 10–30 μm across, are either rounded or shaped like hibonite laths, and some are associated with rhönite in a texture that looks like a reaction rim (Fig. 1b). Lath-shaped grains that are part-spinel and part-hibonite can also be found. Hibonite laths are typically ~20 μm long and ~5 μm across. They are commonly corroded where they are in contact with melilite, but hibonite-spinel contacts are straight and fresh-looking (Fig. 1c). Some regions of the inclusion are very hibonite-rich and are dominated by sprays of crystals. Some melilite-rich regions contain 5–10 μm grains of subhedral corundum that are associated with hibonite, grossular and nepheline (Fig. 1d). Rare, ~5 μm , anhedral grains of nearly pure CaTs (Ca-Tschermak's molecule, $\text{CaAl}_2\text{SiO}_6$) pyroxene can be found enclosed in grossular. Locally, perovskite is enclosed in Ti-bearing pyroxene. An accretionary rim, thinnest on smooth nodule surfaces and thickest in embayments, is dominated by andradite, wollastonite, and aluminous, FeO-bearing clinopyroxene.

Sample ALH2 (Fig. 1e) is less "fluffy" than ALH1 but also quite irregularly-shaped. It appears in thin section as two pieces

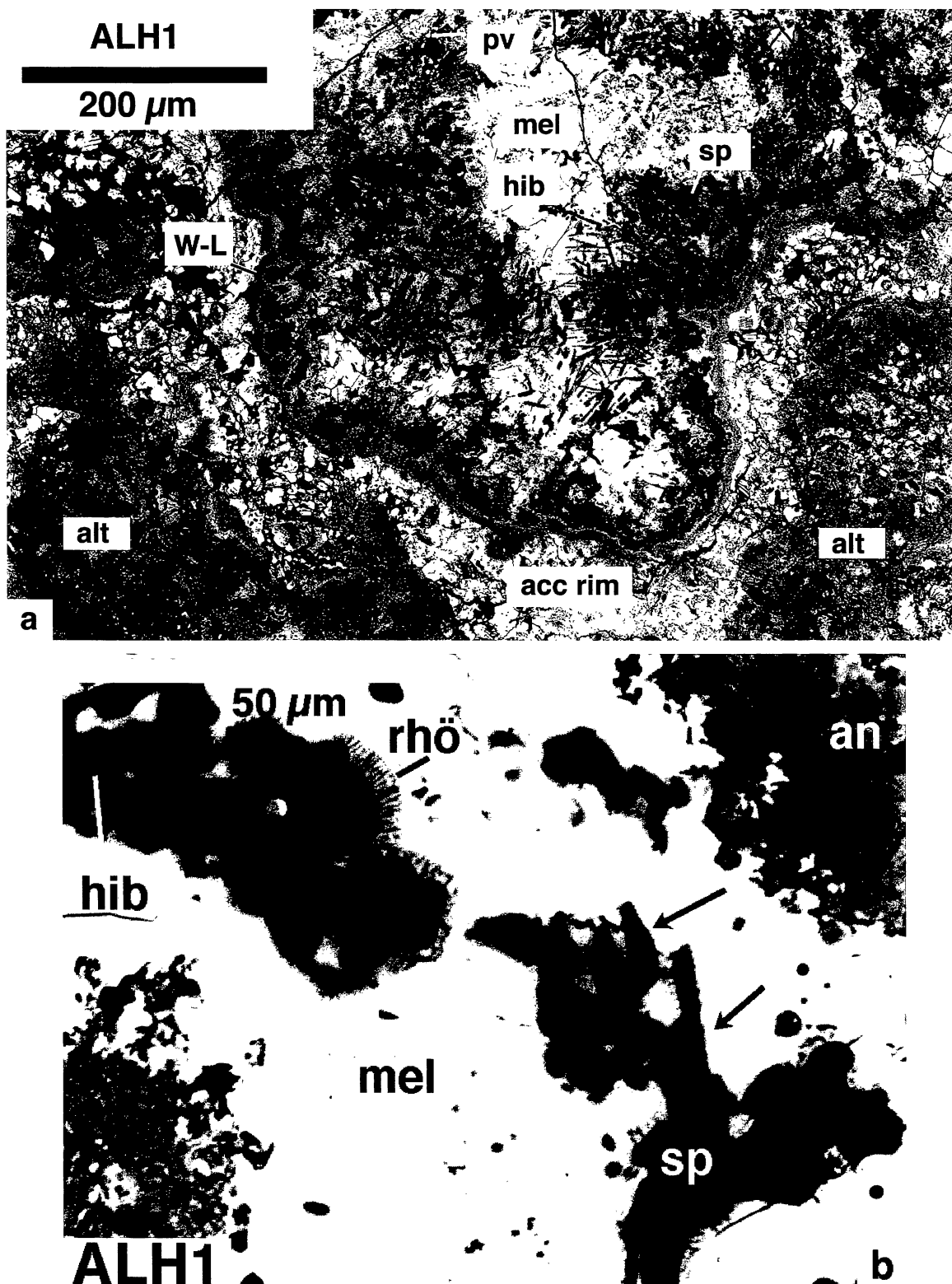


FIG. 1. Backscattered electron images of hibonite-bearing inclusions. (a) ALH1. A hibonite-rich nodule (center), with a prominent Wark-Lovering rim and an adjacent accretionary rim. Parts of other, more heavily-altered nodules of the inclusion are visible at the lower left and lower right corners. (b) ALH1. Lath-shaped (arrowed) and corroded spinel with rims of Al-rich rhönite, enclosed in melilite. Abbreviations: acc rim = accretionary rim; alt = alteration products; an = anorthite; c = corundum; di = diopside; gr = grossular; hib = hibonite; mel = melilite; mtx = matrix; neph = nepheline; pv = perovskite; rhö = rhönite; sp = spinel; W-L = Wark-Lovering rim. *Figure 1 is continued on the next page.*

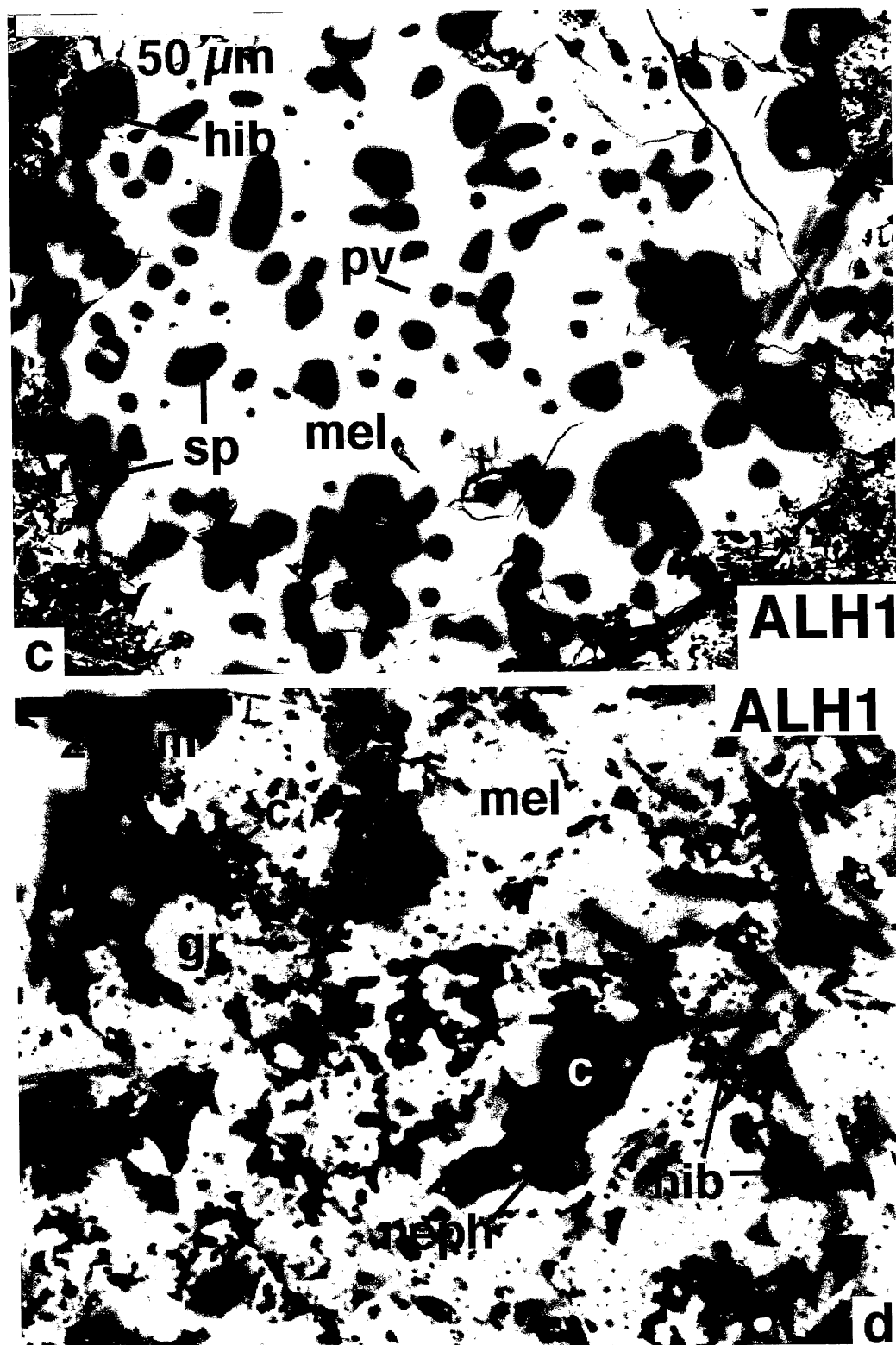


FIG. 1. *Continued.* Backscattered electron images of hibonite-bearing inclusions. (c) ALH1. Corroded hibonite and spinel enclosed in melilite. Note sharp, straight hibonite-spinel contacts. (d) Corundum grains in ALH1. Note straight, angular crystal faces in contact with secondary alteration products. Similar grains occur in ALH2. Abbreviations: acc rim = accretionary rim; alt = alteration products; an = anorthite; c = corundum; di = diopside; gr = grossular; hib = hibonite; mel = melilite; mtx = matrix; neph = nepheline; pv = perovskite; rhö = rhönite; sp = spinel; W-L = Wark-Lovering rim.

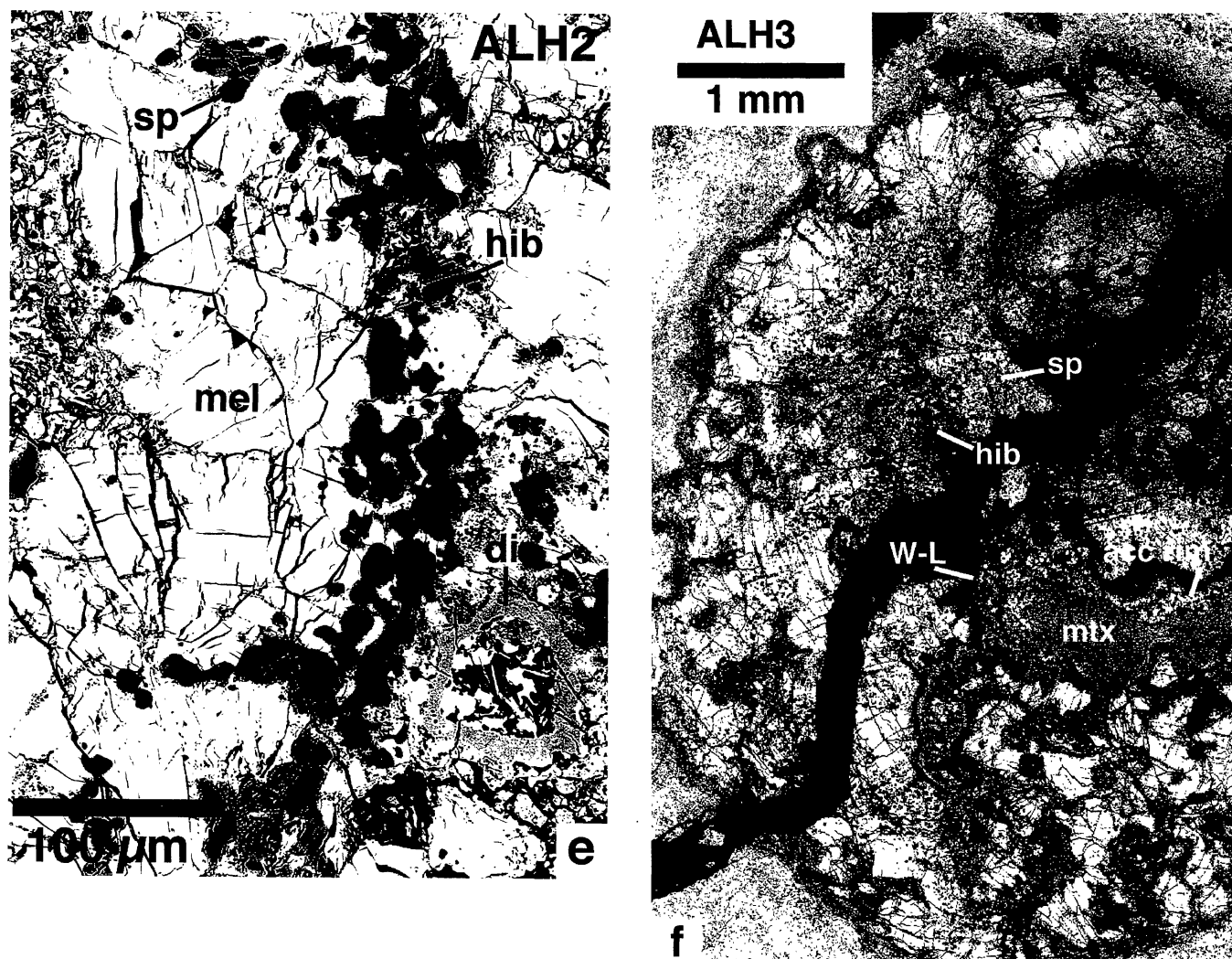


FIG. 1. *Continued.* Backscattered electron images of hibonite-bearing inclusions. (e) ALH2. Portion of a hibonite-, spinel-rich band. Aureole of aluminous diopside (lower right) encloses void space, andradite, and needles of wollastonite. (f) View of most of ALH3. Note rounded shape of the inclusion, melilite-rich outer region, and pocket with accretionary rim and matrix. An epoxy-filled crack cuts across the section. Abbreviations: acc rim = accretionary rim; alt = alteration products; an = anorthite; c = corundum; di = diopside; gr = grossular; hib = hibonite; mel = melilite; mtx = matrix; neph = nepheline; pv = perovskite; rhö = rhönite; sp = spinel; W-L = Wark-Lovering rim.

that are (or were) probably connected outside of the plane of the section. It consists of several millimeter-sized nodules enclosed in Wark-Lovering rims. As in ALH1, hibonite and spinel are rounded where they are in contact with melilite, but hibonite-spinel contacts are straight. Another similarity with ALH1 is that isolated grains of corundum are present, again associated with secondary alteration products. Melilite ranges from small, prismatic grains 40–70 μm across to anhedral grains ~200 μm across. Alteration products, dominated by grossular, are present along many melilite grain boundaries. Hibonite plates are subhedral to anhedral and are mostly 20–50 μm across. Hibonite is very unevenly distributed. Most regions of the inclusion are either hibonite-rich or hibonite-free. One nodule, partially enclosed in another one and defined by an arcuate band of hibonite + spinel (part of which is shown in

Fig. 1e), is more hibonite-rich than the others. Spinel is mostly anhedral (rounded) and ~20 μm across. Areas up to ~200 μm across are locally rich in perovskite. Also present in this sample and in ALH3 are aureoles of aluminous diopside that enclose andradite, wollastonite needles and void space. One of these aureoles can be seen at the lower right in Fig. 1e. Wollastonite needles, along with euhedral grossular, were also found in cavities in CG-11 (Allen *et al.*, 1978). An accretionary rim like that shown in Fig. 1a is present between nodules of the inclusion.

Inclusion ALH3 has an overall rounded shape (Fig. 1f), but its contact with the matrix is irregular and embayed. The inclusion encloses a pocket of matrix and accretionary rim material (hedenbergite, andradite, Al-diopside), and has a Wark-Lovering rim where it is in contact with the matrix pocket

as well as along its exterior. The inclusion is not nodular and the melilite is coarser-grained (200–700 μm) than that in ALH1 and ALH2. There are some laths, but most melilite is present as interlocking anhedral grains. Most grains enclose spinel, but some are spinel-free, and others have both spinel-rich and spinel-poor regions. Like the other two inclusions, unaltered regions of ALH3 are either completely melilite or consist of spinel + hibonite or sprays of hibonite crystals enclosed in melilite. In ALH3, the isolated spinel grains are less rounded than those in ALH1 and ALH2. One grain of fassaite, $75 \times 50 \mu\text{m}$, was found in ALH3.

Mineral Chemistry

Hibonite—Representative analyses of hibonite in the present samples are given in Table 1, and the data are compared to analyses of hibonite from Murchison in Fig. 2. All Ti is reported as TiO_2 . We have not attempted to calculate Ti^{3+} contents from the electron probe data as we do for fassaite (Beckett, 1986; Simon *et al.*, 1991). To do so for hibonite would require that we assume that it always contains 13 cations per 19 oxygen anions; according to Beckett *et al.* (1988), that is not a good assumption because cation defects and oxygen vacancies are possible. We can, however, find evidence for Ti^{3+} in electron probe analyses. End-member hibonite is $\text{CaAl}_{12}\text{O}_{19}$, but Si and Ti^{4+} can enter hibonite *via* a coupled substitution with Mg for 2Al^{3+} , so on a plot of Mg vs. Ti + Si cations, analyses of hibonite generally fall along a 1:1 correlation line. The Allende

TABLE 1. Electron microprobe analyses of hibonite in Allende inclusions.

	ALH1	ALH1	ALH2	ALH2	ALH3	ALH3
MgO	2.36	3.43	2.62	2.97	1.66	3.63
Al ₂ O ₃	82.57	80.05	82.25	82.05	85.87	79.70
SiO ₂	0.18	0.09	0.20	0.09	0.04	0.11
CaO	8.56	8.59	8.58	8.65	8.66	8.55
TiO ₂	4.97	7.47	5.11	6.11	3.21	7.54
V ₂ O ₃	1.55	0.63	1.08	0.48	0.87	0.67
FeO	0.06	0.11	0.03	0.03	BLD	BLD
Total	100.25	100.37	99.87	100.38	100.31	100.20

Cations per 19 oxygen anions

Mg	0.400	0.579	0.443	0.499	0.278	0.615
Al	11.040	10.688	11.006	10.906	11.378	10.657
Si	0.020	0.010	0.023	0.011	0.004	0.012
Ca	1.041	1.042	1.044	1.045	1.043	1.040
Ti	0.424	0.637	0.436	0.518	0.271	0.644
V	0.070	0.029	0.049	0.022	0.039	0.030
Fe	0.006	0.010	0.003	0.003	0	0
Total	13.001	12.995	13.004	13.004	13.013	12.998

All Ti reported as TiO_2 . BLD = below limit of detection of 0.030 wt% for FeO.

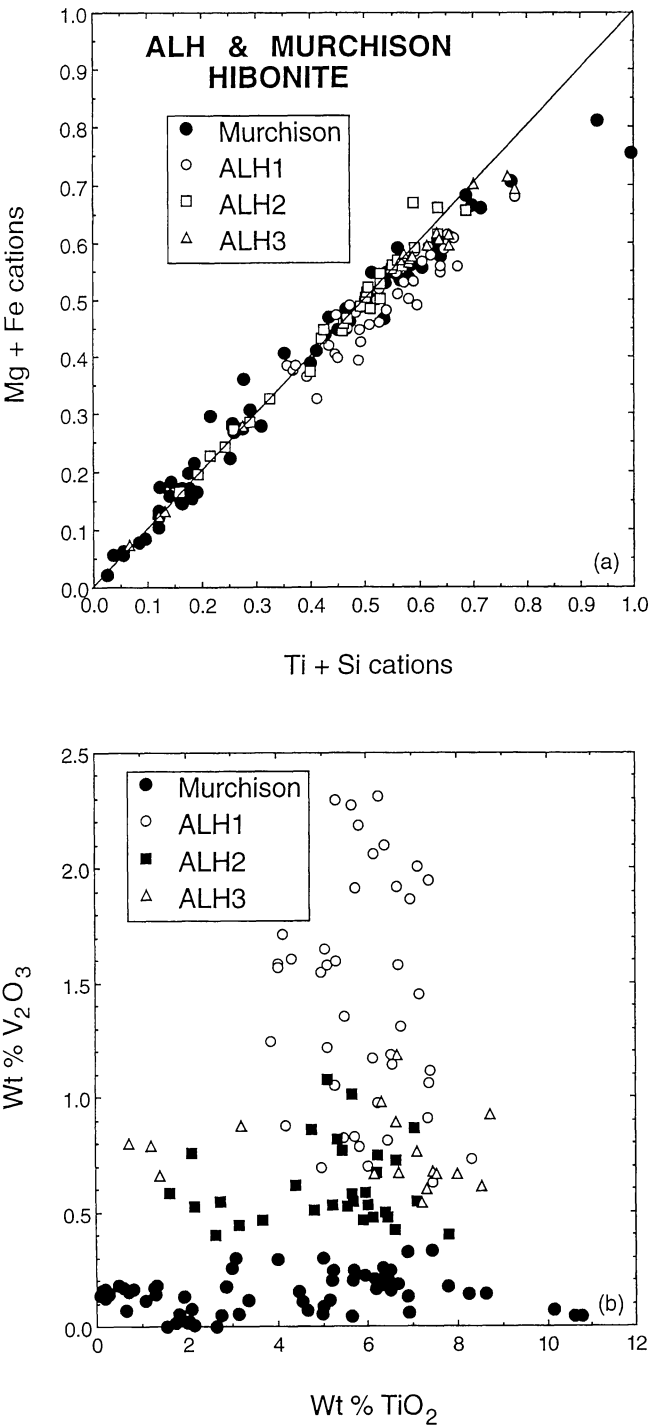


FIG. 2. Compositions of ALH hibonite compared to those from Murchison. (a) Mg + Fe vs. Ti + Si, cations per 19 oxygens. Allende hibonite plots on the 1:1 correlation line or slightly to the Ti + Si-rich side, exhibiting much overlap with analyses of hibonite from Murchison. (b) V_2O_3 vs. TiO_2 , wt%. These oxides are not correlated with each other in either Murchison or Allende hibonite, but the latter has much higher V_2O_3 contents than the former. Murchison data are from Simon *et al.* (1997) and unpublished data of the authors.

hibonite contains minor amounts of FeO, which most likely replaced MgO, so we have plotted Mg + Fe vs. Si + Ti in Fig. 2a. Because Ti^{3+} can substitute directly for Al, any additional Ti in this oxidation state will cause an analysis to plot off the 1:1 line, to the Ti-rich side. Wide ranges of Ti contents are seen within each of the ALH samples and within some single crystals. Most of the analyses of hibonite from ALH2, like that in some Murchison inclusions (Simon *et al.*, 1997), plot on the 1:1 line. Hibonite analyses from ALH1 and ALH3 either plot on the 1:1 line or follow the Murchison trend away from it, to the Ti-rich side. They therefore probably originally contained Ti^{3+} .

The Allende hibonite contrasts sharply with that from Murchison with respect to V_2O_3 contents, which are summarized in Fig. 2b. The hibonite in all three samples considered here has much higher V_2O_3 contents than hibonite from Murchison. As the plot shows, V_2O_3 and TiO_2 contents are not correlated in either Murchison or Allende. Hibonite in ALH1 has quite high V_2O_3 contents, with most analyses >1 wt%. The range of V_2O_3 contents observed in ALH2 and ALH3 hibonite, ~0.5–1.2 wt%, is similar to that seen in CAI 3643, an inclusion from Allende in which the hibonite has a range of 0.11–1.31 wt% V_2O_3 , with a mean of 0.73 wt% (Wark, 1986). Allen *et al.* (1978) reported an average V_2O_3 content of 0.35 wt% for the hibonite in CG-11, which is also higher than typically observed in Murchison hibonite. Ihinger and Stolper (1986) noted that the presence of V was essential for the development of orange color in hibonite, and that V_2O_3 -rich (~1.1 wt%) hibonite remained orange to a lower $f\text{O}_2$ than did V_2O_3 -poor (0.38 wt%) hibonite.

Hibonite is quite rare among calcium-aluminum-rich inclusions (CAIs) in meteorite types other than CM. Analyses of hibonite in CAIs from Allan Hills (ALH) 85085 (CH), Lancé (CO), and Yamato (Y)-791717 (CO) yield low TiO_2 and V_2O_3 contents (Brearley and Jones, 1998).

Melilite—The range of melilite compositions in these inclusions is quite similar to that found in the suite of Allende fluffy Type A inclusions studied by MacPherson and Grossman (1984). For the 13 inclusions they studied, MacPherson and Grossman (1984) reported a range of Åk_{0-33} . We find ranges and means of $\text{Åk}_{0.3-16.3}$ and Åk_6 for ALH1 (68 analyses), $\text{Åk}_{0.8-23.9}$ and Åk_{14} for ALH2 (251 analyses), and $\text{Åk}_{1.1-29.2}$ and Åk_{12} in ALH3 (137 analyses). These ranges clearly do not extend to the relatively Åk -rich compositions that can be found in most compact Type A (Simon *et al.*, 1999) and Type B inclusions (Grossman, 1980).

Unlike that in ALH1, the melilite in ALH2 and ALH3 is coarse enough for measurement of zoning profiles by electron microprobe. It does not exhibit trends of increasing Åk content with distance from the crystal cores that would result from closed-system fractional crystallization of melilite from aluminous melts. Like some of the fluffy Type A inclusions described by MacPherson and Grossman (1984), ALH2 contains reversely zoned melilite, with Åk -poor rims and

relatively Åk -rich cores. The results of two traverses are shown in Fig. 3. The melilite in ALH3 typically has no dominant core-rim trend. Several of the grains we investigated have zoning patterns that resemble the sawtooth pattern seen in melilite from TS12, an Allende compact Type A (CTA) inclusion (Simon *et al.*, 1999).

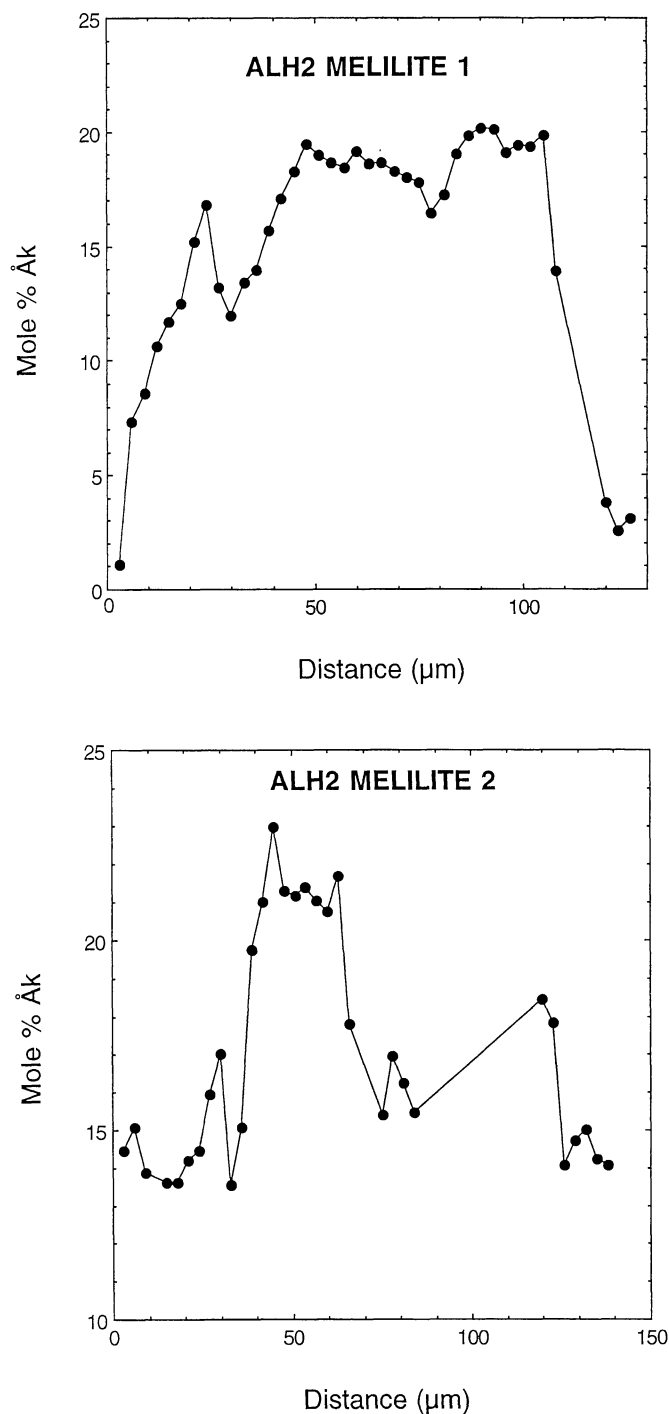


FIG. 3. Results of rim-to-rim electron probe traverses across melilite grains in ALH2. Note the relatively Åk -rich cores and Åk -poor rims.

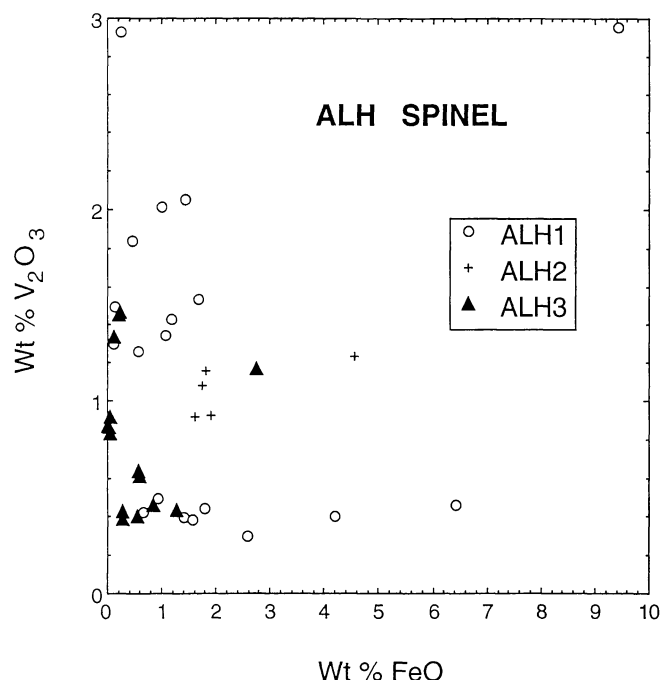


FIG. 4. V_2O_3 and FeO contents in ALH spinel. Like many fluffy Type A inclusions, V_2O_3 contents are high and are not correlated with FeO.

Spinel—MacPherson and Grossman (1984) noted that spinel in fluffy Type A inclusions tended to be V-rich, with spinels within single inclusions exhibiting wide ranges of V_2O_3 and FeO contents. The abundances of these oxides in the spinel in the present samples are summarized in Fig. 4. We also note high V_2O_3 contents, with wide ranges in ALH1 and ALH3. We observe no correlation between FeO and V_2O_3 , supporting the conclusion of MacPherson and Grossman (1984) that the high V_2O_3 contents of the grains are not related to the late addition of FeO. The lath-shaped spinel generally has V_2O_3 and TiO_2 contents that are low but within the range of those of the other spinels.

Fassaite—One grain of Ti-rich fassaite was found, in ALH3. It is complexly zoned with respect to Ti contents, with three irregularly shaped zones that have from 11–12 wt% $TiO_2 + Ti_2O_3$ in the "low-Ti" zone, 14.5–16.6 wt% in the "medium-Ti" zone, and 17–19 wt% in the "high-Ti" zone. The high-Ti zone dominates the outer region of the grain, so we can say that the grain is reversely zoned compared to what we might expect from fractional crystallization of a typical CAI composition (Simon *et al.*, 1991). Representative analyses of each zone are given in Table 2. The composition of this grain is not like typical fassaite from either Type B (Simon *et al.*, 1991) or CTA (Simon *et al.*, 1999; Nazarov *et al.*, 2000) inclusions. As illustrated in Fig. 5, it is more Ti-rich than Type B fassaite, and is Sc_2O_3 -poor compared to fassaite from CTAs that have the same or even higher V_2O_3 contents. The medium-Ti zone of the ALH3 grain has a wide range of V_2O_3 contents, and V_2O_3 contents of the low- and high-Ti zones fall within

TABLE 2. Electron microprobe analyses of fassaite in ALH3.

	Low-Ti	Medium-Ti	High-Ti
MgO	6.25	3.99	3.25
Al_2O_3	22.20	26.12	25.81
SiO_2	32.63	27.52	25.96
CaO	24.72	24.70	24.42
Sc_2O_3	0.05	0.14	0.12
TiO_2^{tot}	13.02	16.23	20.10
V_2O_3	1.01	1.43	1.16
FeO	0.05	0.02	0.03
Ti_2O_3	8.20	9.54	12.59
TiO_2	3.98	5.83	6.28
Total	99.09	99.29	99.62
Cations per 6 oxygen anions			
Si	1.243	1.063	1.007
Al	0.757	0.937	0.993
Tet. sum	2.000	2.000	2.000
Al	0.240	0.252	0.187
Mg	0.355	0.230	0.188
Ca	1.000	1.000	1.000
Sc	0.002	0.005	0.004
Ti^{3+}	0.260	0.304	0.404
Ti^{4+}	0.113	0.167	0.182
V	0.029	0.041	0.034
Fe	0.002	0.001	0.001
Oct. sum	2.001	2.000	2.000

Analyses are normalized to four cations, including two tetrahedral cations and one Ca cation, per six O anions according to the methods of Beckett (1986).

this range. This fassaite is also more Al_2O_3 -rich than that from most other refractory inclusions.

Other Phases—The other phases found in these samples include essentially end-member perovskite, corundum, grossular, anorthite, andradite, and wollastonite. Analyses of rhönite adjacent to the lath-shaped spinel shown in Fig. 1b are given in Table 3. It is quite Al-rich and Ti-poor compared to previously reported occurrences in Allende (*e.g.*, Fuchs, 1971; Simon *et al.*, 1999) and to rhönite synthesized at sub-solar oxygen fugacities (Beckett, 1986). Another interesting phase, found in ALH1, is nearly pure Ca-Tschermak's molecule (Table 4). Pyroxene with up to ~80 mol% CaTs has been reported from some hibonite-pyroxene spherules (*e.g.*, Simon *et al.*, 1998b); we found four grains in ALH1 with 92–99 mol% CaTs.

Major Element Bulk Compositions

We calculated the bulk compositions of the inclusions from modal abundances, densities (Beckett, 1986) and average

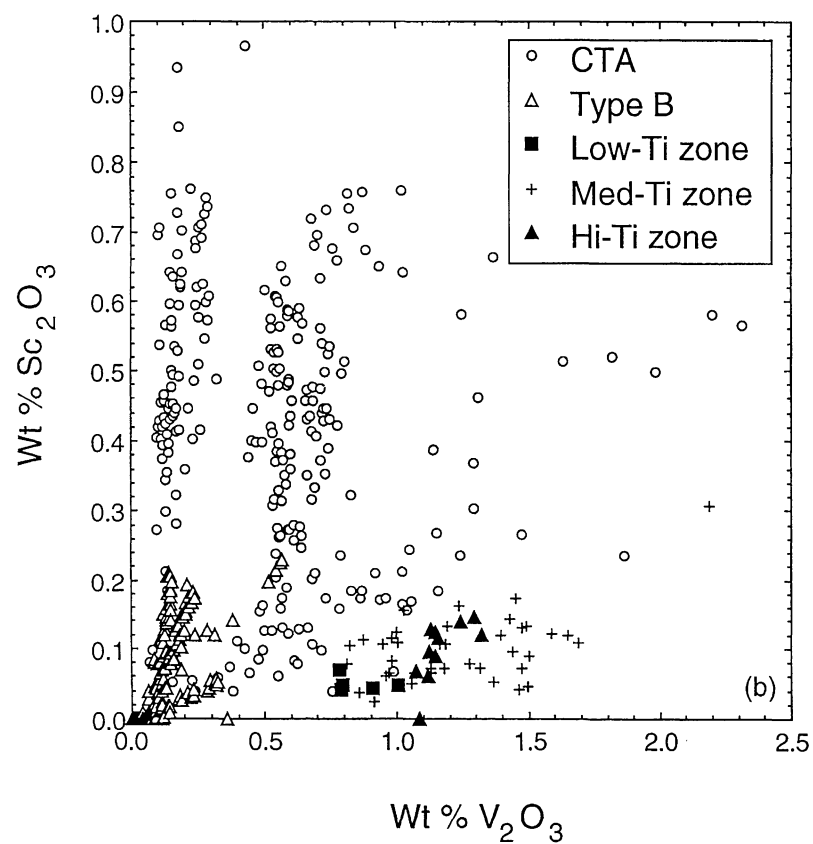
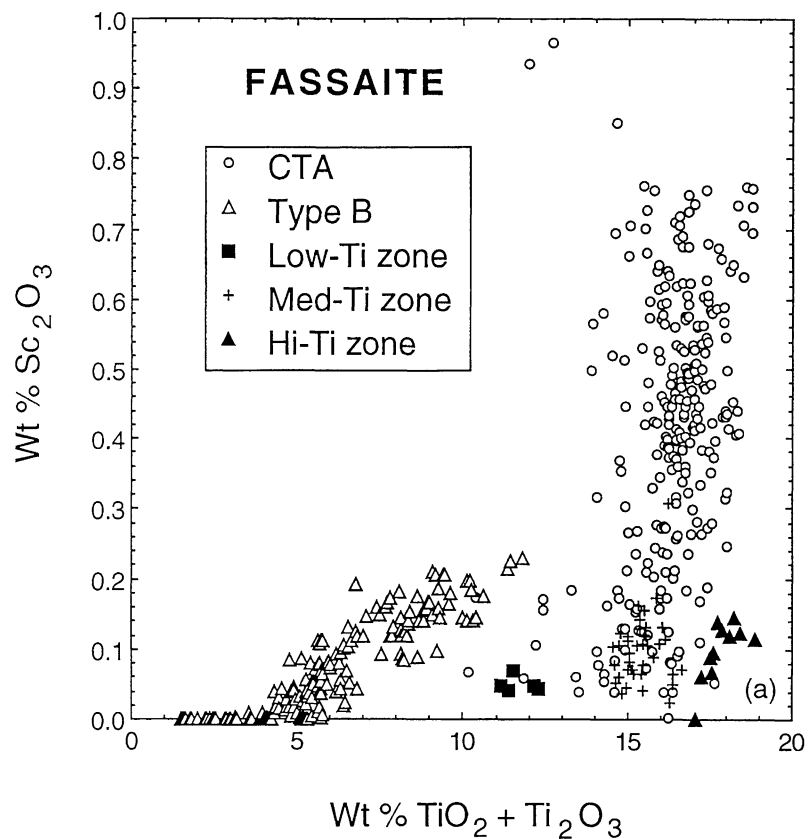


FIG. 5. Compositions of fassaite in ALH3 compared to those of fassaite in compact Type A and Type B inclusions. Compared to that in Type A inclusions, fassaite in the present sample is V-rich and has low Sc contents. Compared to that in Type B inclusions, fassaite in the present sample is Ti- and V-rich and has similar Sc contents. (a) Sc_2O_3 vs. $\text{TiO}_2 + \text{Ti}_2\text{O}_3$. (b) Sc_2O_3 vs. V_2O_3 . Data for Type A fassaite are from Simon *et al.* (1999); for Type B fassaite, from Simon *et al.* (1991).

compositions of the phases. Modal abundances were determined from automated traverses conducted with the SEM, following grid patterns that covered the entire inclusions. Approximately 1000 quantitative energy-dispersive analyses were collected per sample, but many had to be discarded due to the irregular shapes of, and matrix pockets within, the inclusions, especially ALH1. After removal of analyses of matrix, cracks, and epoxy, this left 273 points for ALH1, 466 points for ALH2, and 467 points for ALH3. We assumed that the alteration products now present were formed from melilite, and, after Beckett (1986), that the altered melilite had the same average composition as that remaining in the inclusion. Results are summarized in Table 5. Compared to the literature data compiled by Grossman *et al.* (2000), these compositions are at the high- Al_2O_3 , low-MgO ends of the ranges for Type A inclusions. The composition of ALH1 is very similar to that

reported for CG-11 (Allen *et al.*, 1978). When the bulk compositions of the inclusions are projected from spinel onto the gehlenite–forsterite–anorthite plane in the $\text{CaO-MgO-Al}_2\text{O}_3\text{-SiO}_2$ system following the method of Stolper (1982), all three ALH inclusions plot near the gehlenite apex. Based on experimentally determined phase relations (Stolper, 1982;

TABLE 3. Electron microprobe analyses of rhönite in ALH1.

	1.	2.
MgO	12.84	12.48
Al_2O_3	42.46	42.57
SiO_2	19.19	18.82
CaO	16.59	17.99
$\text{TiO}_2^{\text{tot}}$	9.17	7.83
Sc_2O_3	0.27	0.15
V_2O_3	0.76	0.70
Cr_2O_3	0.07	0.13
FeO	0.28	0.81
Ti_2O_3	6.30	2.99
TiO_2	2.17	4.51
Total	100.93	101.15

Cations per 40 oxygen anions

Si	4.708	4.615
Al	7.292	7.385
Tet. sum	12.000	12.000
Al	4.986	4.920
Mg	4.695	4.560
Ca	4.361	4.726
Sc	0.057	0.032
Ti^{3+}	1.293	0.613
Ti^{4+}	0.400	0.832
V	0.140	0.129
Cr	0.013	0.024
Fe	0.057	0.166
Oct. sum	16.002	16.002

Analyses are normalized to 28 cations, including 12 tetrahedral cations, per 40 O anions by a method analogous to that used for fassaite (Beckett, 1986).

TABLE 4. Electron microprobe analyses of CaTs in ALH1.

	1.	2.
MgO	0.61	0.19
Al_2O_3	44.84	45.28
SiO_2	27.78	27.39
CaO	25.70	26.07
TiO_2	0.36	0.06
FeO	0.39	0.26
Total	99.68	99.25

Cations per 6 oxygen anions

Si	1.015	1.006
Al	0.985	0.994
Tet. sum	2.000	2.000
Al	0.947	0.966
Mg	0.033	0.010
Ca	1.006	1.026
Ti	0.010	0.001
Fe	0.012	0.008
Oct. sum	2.008	2.011
Di	3.35	1.07
CaTs	95.65	98.78
TPx	1.00	0.15

TABLE 5. Bulk compositions of ALH inclusions.

	ALH1	ALH2	ALH3
MgO	5.1	4.3	6.4
Al_2O_3	44.6	38.5	41.4
SiO_2	16.5	20.4	19.0
CaO	31.7	35.6	32.9
TiO_2	2.1	1.2	0.3
Avg. mel	$\text{\AA}k_6$	$\text{\AA}k_{14}$	$\text{\AA}k_{12}$
Fo	-2.5	3.6	3.8
An	1.4	-0.4	-0.1
Ge	101.1	96.8	96.3
Sp	22.2	8.8	16.1

Fo, An, and Ge represent the coordinates for projection from spinel (Sp) onto the forsterite–anorthite–gehlenite plane, according to the method of Stolper (1982).

Beckett and Stolper, 1994), spinel is the predicted liquidus phase for each inclusion, followed by melilite. All three compositions plot well below the hibonite saturation surface of Beckett and Stolper (1994), which means that hibonite should not be a near-liquidus (early-crystallizing) phase from melts of these compositions.

Trace Element Abundances

Trace element abundances within individual phases were determined by ion microprobe. Analyses of major phases are given in Table 6, and chondrite-normalized REE abundance patterns are illustrated in Fig. 6. Fairly clean analyses of melilite and hibonite were obtained in all three ALH inclusions, but perovskite was too fine-grained to allow clean analyses. One perovskite-rich spot was analyzed in each inclusion, and the bulk spot analyses are given in Table 6. For each of these spots, the proportions of phases were calculated from the major element concentrations as determined by ion microprobe. The perovskite-bearing spots in ALH1, ALH2 and ALH3 contain 10, 35 and 80% perovskite, respectively. Since perovskite is

quite rich in REE compared to melilite and hibonite, we normalized the REE abundances in the perovskite-bearing analysis spot to the fraction of perovskite present in order to obtain the perovskite REE patterns that are shown in Fig. 6. No negative Ce anomalies were found in any phase in any of the ALH inclusions.

In ALH1, hibonite has unusually low REE contents and is enriched in heavy (HREE) relative to light REE (LREE). Melilite is only slightly enriched in heavy relative to LREE, with overall abundances of $\sim 10 \times \text{CI}$ and a positive Eu anomaly. Perovskite is also enriched in heavy relative to LREE, with CI-normalized enrichment factors ranging from 400 to 1500, and has a negative Eu anomaly.

In ALH2, hibonite and melilite have comparable REE enrichment patterns, with hibonite slightly more enriched in LREE and melilite in HREE. Melilite has a positive Eu anomaly that is somewhat larger than the one in ALH1 melilite. Perovskite is enriched in heavy relative to LREE, but overall enrichments are not as high as in ALH1 perovskite.

In ALH3, all phases analyzed exhibit fractionated, Group II-like patterns, with mostly flat LREE abundances that are

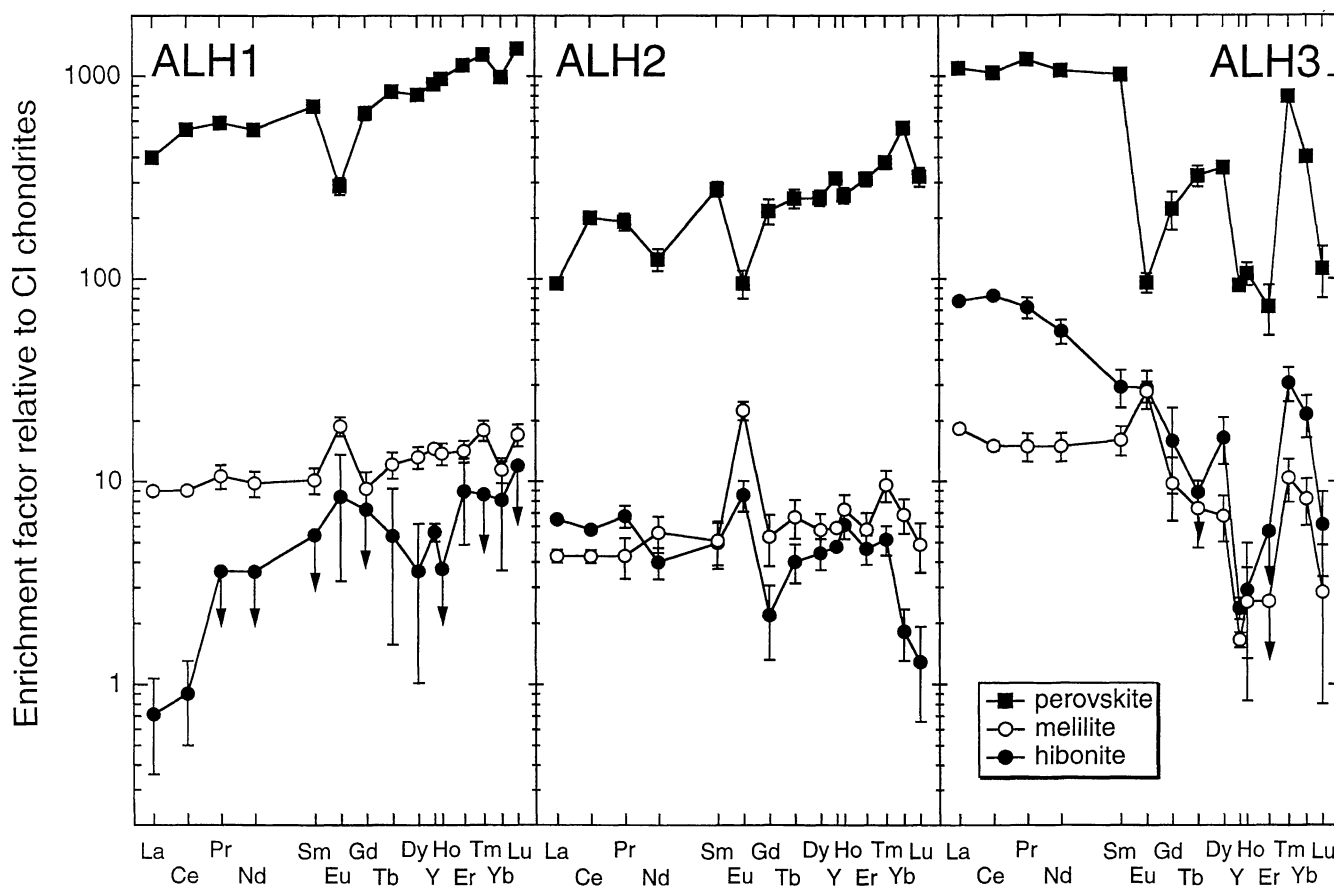


FIG. 6. Chondrite-normalized REE enrichment factors in ALH1, ALH2 and ALH3. Melilite and hibonite patterns in each CAI are based on 1 to 3 spot analyses. The perovskite patterns are based on one spot analysis of a perovskite-rich area in each CAI and were calculated from the REE patterns of the spots and the modal proportions of perovskite calculated from the major element contents of the corresponding analytical volumes. Uncertainties are 1σ , based on counting statistics. Downward-pointing arrows indicate cases where upper limits (2σ) have been plotted.

TABLE 6. Major and trace element abundances in hibonite, melilite and perovskite-rich spots.*

Phase #	ALH1	ALH1	ALH1	ALH2	ALH2	ALH2	ALH2	ALH3	ALH3
	$\hat{A}k_{6.5}$ ₂	hib 1	hib,mel,pv,sp 1	$\hat{A}k_{9.0}$ ₂	hib 3	hib,pv,mel 1	$\hat{A}k_{11.7}$ ₁	hib 1	pv,mel,hib 1
MgO (wt%)	0.045 ± 0.010	0.567 ± 0.107	0.461 ± 0.032	0.080 ± 0.014	0.311 ± 0.021	0.314 ± 0.048	0.040 ± 0.013	8.14	0.132 ± 0.031
Al ₂ O ₃ (wt%)	1.10	1.83	2.54	1.27	2.70	2.74	1.60	3.23	1.03
SiO ₂ (wt%)	35.2	85.4	63.2	33.7	81.4	36.1	32.5	83.1	5.84
CaO (wt%)	23.4	1.46	10.1	23.9	1.35	12.2	24.4	0.47	6.03
TiO ₂ (wt%)	39.8	7.03	14.8	40.9	8.64	24.6	41.3	6.83	39.9
	0.051	2.49	7.26	0.088	5.06	22.1	0.072	5.68	46.5
Li									
Be									
B									
Na									
K									
Sc									
V									
Cr									
Mn									
Fe									
Co									
Rb									
Sr									
Y									
Zr									
Nb									
Ba									
La									
Ce									
Pr									
Nd									
Sm									
Eu									
Gd									
Tb									
Dy									
Ho									
Er									
Tm									
Yb									
Lu									
Th									
U									

*Determined by ion microprobe (in ppm unless otherwise indicated). Where multiple analyses were available, averages are given. Errors are $\pm 1\sigma$ based on counting statistics, and are only given where they exceed 5% of the amount present; upper limits are $<2\sigma$. Abbreviations: hib = hibonite, mel = melilite, pv = perovskite, sp = spinel.

enriched relative to the HREE and $\text{Tm} \gg \text{Er}$. Hibonite is significantly enriched in LREE compared to melilite. Melilite has a small positive Eu anomaly. Perovskite is quite high in REE, with LREE and Tm enrichments of $\sim 1000 \times \text{CI}$ in a well-defined Group II pattern.

In contrast with the present samples, much of the Murchison hibonite analyzed by Ireland *et al.* (1988) has much higher abundances, with typical LREE enrichment factors of $\sim 100 \times \text{CI}$ and negative Eu anomalies. The Allende hibonite especially differs from the coarse (70–150 μm) single crystals of hibonite from Murchison with respect to Yb/Lu ratios. In the present samples, chondrite-normalized Lu abundances are less than or within error of the normalized Yb abundances, whereas the coarse Murchison crystals commonly have $\text{Lu} \gg \text{Yb}$ (Ireland *et al.*, 1988).

Isotopic Analyses

The Mg isotopic compositions of phases in each of the inclusions were determined by ion microprobe mass spectrometry. Results are given in Table 7 and illustrated in Fig. 7. Many of the ALH2 and ALH3 analyses show small ^{25}Mg excesses. The primary phases spinel, hibonite and melilite all show ^{26}Mg excesses. As the plots show, most analyses of these phases are consistent with an initial $^{26}\text{Al}/^{27}\text{Al}$ of 5×10^{-5} for each inclusion. Melilite shows some evidence of disturbance, which is not surprising because it is moderately to heavily altered in these inclusions. Corundum in ALH2 does not contain any significant ^{26}Mg excesses, consistent with textural features indicating that in this inclusion, and probably in ALH1 as well, it is not a primary phase. All three hibonite-rich samples have magnesium isotopic compositions that are mass-fractionated in favor of the heavy isotopes. Uncertainties in isotopic compositions are a few permil on each spot, so it is difficult to make a strong case for isotopic heterogeneity within each CAI. The weighted average $\Delta^{25}\text{Mg}$ values of ALH1, ALH2 and ALH3 are 5.1 ± 2.7 , 8.4 ± 1.5 and $10.4 \pm 1.2\%$, respectively. These values are within the range seen in normal, non-FUN, Allende CAIs (Clayton *et al.*, 1988).

DISCUSSION

Origin of Hibonite in These Inclusions

Experiments (Ihinger and Stolper, 1986) and analytical studies (Beckett *et al.*, 1988) have shown that blue hibonite, like that found in refractory inclusions from CM2 chondrites, contains Ti^{3+} , while orange hibonite, like that in Allende, does not. From measurements performed on synthetic orange hibonite, Ihinger and Stolper (1986) concluded that Allende hibonite equilibrated at $f\text{O}_2 \geq 10^{-8}$ at 1700 K (IW+1), at least seven orders of magnitude more oxidizing than is expected for the solar nebula. Because such conditions seemed unreasonable, Ihinger and Stolper (1986) suggested that Allende hibonite

could have formed under typical, reducing conditions in the nebula and re-equilibrated later at a relatively high oxygen fugacity. The ambient oxygen fugacity at the time of formation can affect some of the chemical characteristics of hibonite, so clues to its formation conditions can be obtained from its major and trace element abundances.

Evidence from Ti-Mg Relationships—If all Ti in the hibonite of the ALH samples were originally Ti^{4+} , then on a plot of $\text{Mg} + \text{Fe}$ vs. $\text{Ti} + \text{Si}$ (Fig. 2a), the analyses would plot on a 1:1 correlation line. If, on the other hand, some of the Ti were originally trivalent, then we would expect the analyses to follow the Murchison trend of plotting on the line at low Ti contents and increasingly diverging from the line with increasing Ti contents. We find that many of the analyses of hibonite from ALH2 plot along the 1:1 line while the ALH1 and ALH3 data plot on the line or to the Ti-rich side and overlap the Murchison analyses, consistent with an original presence of Ti^{3+} .

Ihinger and Stolper (1986) showed that blue hibonite could be converted to orange and back to blue simply by changing the $f\text{O}_2$ at 1700 K. This suggests that oxidation and reduction of Ti can occur *in situ* in hibonite. It seems unlikely that this change is accompanied by substitution of additional cations, as this would have required Al and Mg cations to have been available for each $f\text{O}_2$ change in the experiments, and to diffuse in and out of the crystals in response to these changes. Also, the color change can occur rapidly, in as little as one hour at 1700 K (Ihinger and Stolper, 1986), and even during quenching of an experimental run product (Ihinger and Stolper, 1986; Beckett *et al.*, 1988), making a coupled cationic substitution appear unlikely. A mechanism by which Ti^{4+} in hibonite can be reduced *in situ* without coupled substitution of other cations for charge balance was described by Beckett *et al.* (1988). Briefly, when the ambient $f\text{O}_2$ decreases, oxygen anions can be removed from the hibonite lattice as O gas, leaving behind one doubly-charged (2+) oxygen site and two electrons per anion removed. The free electrons can then convert two Ti^{4+} to two Ti^{3+} cations. When the ambient $f\text{O}_2$ increases, the reverse happens, with oxygen entering the lattice and oxidizing Ti^{3+} . Beckett *et al.* (1988) noted that their data were consistent with this mechanism and that doubly ionized oxygen vacancies are known to occur in other oxides. Perhaps charge-balancing by oxygen diffusion occurs more readily than cation diffusion in hibonite because it is easier than simultaneous diffusion of Mg and Al. This reaction does not affect the $(\text{Ti} + \text{Si})/(\text{Mg} + \text{Fe})$ cation ratios as measured by the electron probe, so that Ti^{3+} that directly substituted for Al would still appear as excess Ti relative to Mg on Fig. 2a. Importantly, this reaction also would not modify the Mg isotopic composition of the hibonite. If late oxidation were accompanied by substitution of Mg for Al, the isotopic systems would be disturbed and we would not observe ^{26}Mg abundances that are consistent with initial $^{26}\text{Al}/^{27}\text{Al}$ ratios of 5×10^{-5} (Fig. 7). We therefore conclude that ALH hibonite originally contained Ti^{3+} and was later oxidized, while hibonite from Murchison was not.

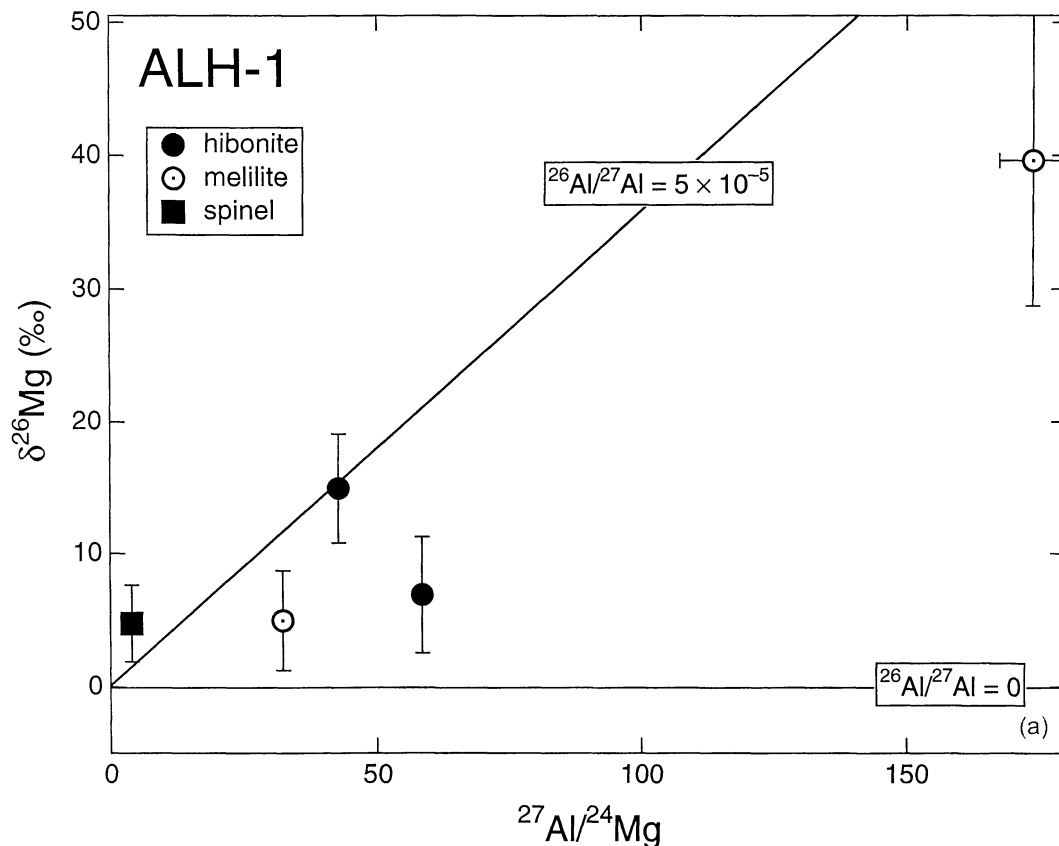
TABLE 7. Magnesium isotopic compositions and $^{27}\text{Al}/^{24}\text{Mg}$ ratios in hibonite-rich Allende CAIs.

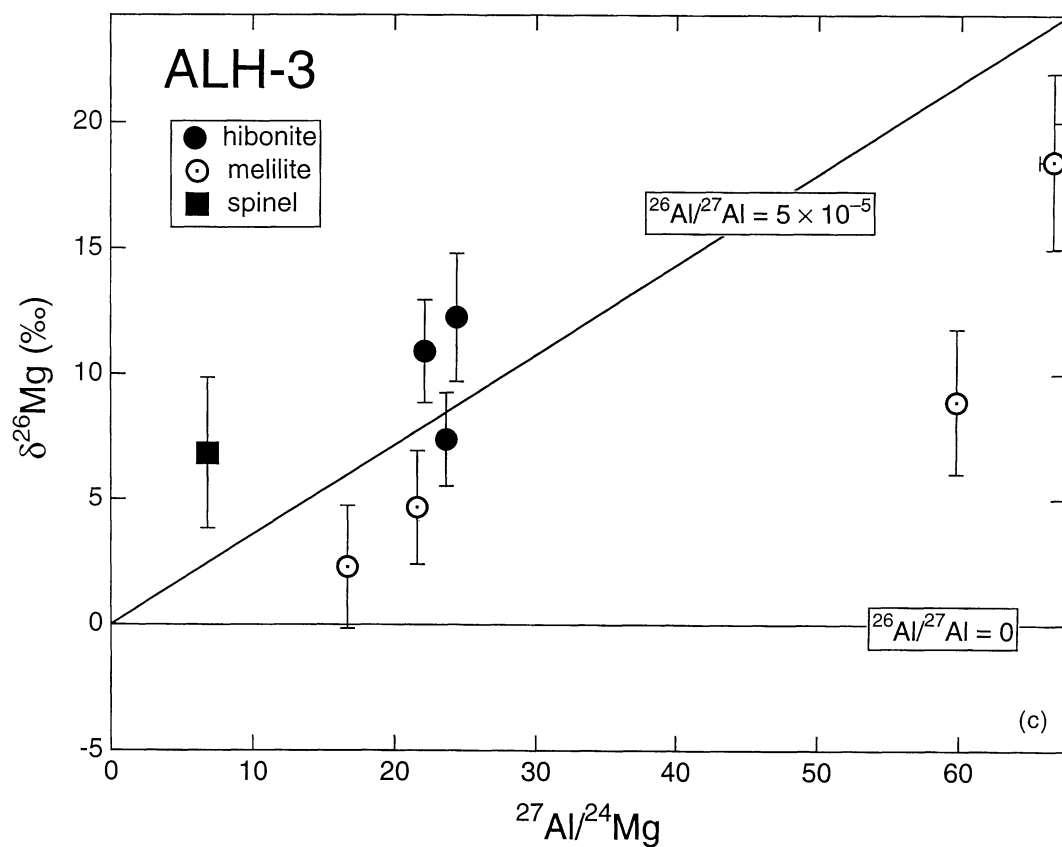
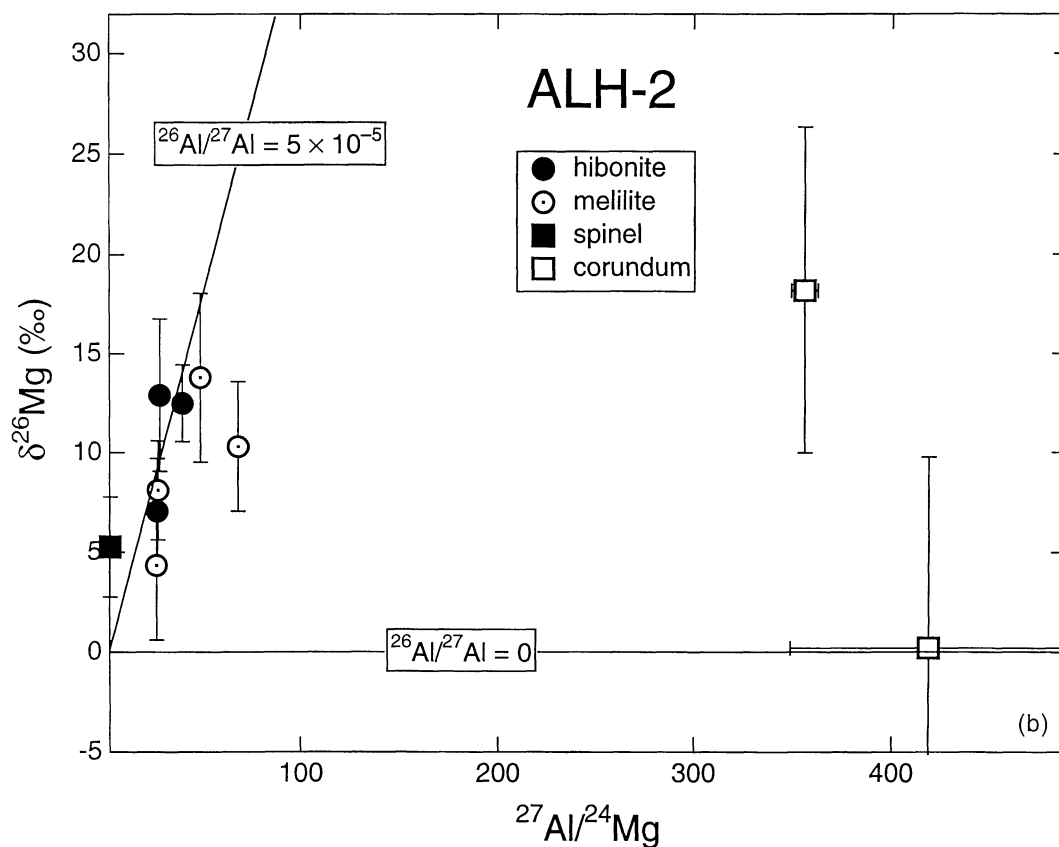
	$^{27}\text{Al}/^{24}\text{Mg}$	$\delta^{26}\text{Mg}$ (‰)	$\Delta^{25}\text{Mg}$ (‰)
ALH1			
hibonite	42.7 ± 1.2	14.9 ± 8.3	4.2 ± 4.7
hibonite	58.5 ± 1.7	6.9 ± 8.7	13.5 ± 9.0
melilite	32.3 ± 0.5	5.0 ± 7.5	6.1 ± 5.7
melilite	174 ± 13	40 ± 22	13 ± 16
spinel	4.1 ± 0.2	4.8 ± 5.7	-0.4 ± 3.8
ALH2			
hibonite	29.3 ± 0.3	12.9 ± 7.7	5.9 ± 5.0
hibonite	28.0 ± 0.4	7.1 ± 5.3	6.9 ± 3.9
hibonite	40.7 ± 0.3	12.5 ± 3.9	10.3 ± 3.0
melilite	68.7 ± 0.9	10.3 ± 6.5	9.4 ± 4.1
melilite	27.6 ± 0.4	4.4 ± 7.4	9.6 ± 4.3
melilite	28.4 ± 0.3	8.1 ± 5.0	4.4 ± 4.0
melilite	49.8 ± 2.4	13.8 ± 8.5	6.5 ± 6.0
cor/gr	356 ± 13	18 ± 16	6 ± 14
cor/gr	419 ± 139	0.2 ± 19	23 ± 11
spinel	4.1 ± 0.2	5.3 ± 5.0	7.9 ± 3.5
ALH3			
hibonite	22.1 ± 0.1	10.9 ± 4.1	13.4 ± 2.9
hibonite	23.7 ± 0.2	7.4 ± 3.7	7.5 ± 2.6
hibonite	24.4 ± 0.2	12.3 ± 5.1	8.5 ± 3.2
melilite	66.6 ± 2.0	18.5 ± 6.9	15.2 ± 6.3
melilite	16.7 ± 0.2	2.3 ± 4.9	8.5 ± 3.4
melilite	21.6 ± 0.1	4.7 ± 4.6	8.9 ± 3.0
melilite	59.8 ± 0.8	8.9 ± 5.8	18.6 ± 3.5
melilite	40.8 ± 2.1	9.7 ± 21.6	0.7 ± 15.2
spinel	6.8 ± 1.2	2.6 ± 6.0	7.3 ± 4.2

Uncertainties are $\pm 2\sigma$. Abbreviation: cor/gr = corundum, grossular.

Evidence from Chondrite-Normalized REE Abundances—Cerium becomes volatile relative to the other REE when it is oxidized to Ce^{4+} . Calculations by Davis *et al.* (1982) predict chondrite-normalized REE patterns with La/Ce ratios of ~ 100 – 300 for solids in equilibrium with C1 gas at 1450 – 1626 K, $P_{\text{tot}} = 10^{-10}$ atm. Based on the calculations of Ebel and Grossman (2000a) for a system with $P_{\text{tot}} = 10^{-6}$ bar and a C1 dust/gas ratio of 1000 , we estimate that the conditions considered by Davis *et al.* (1982) correspond to oxygen fugacities approximately equivalent to IW. These values are ~ 6 orders of magnitude more oxidizing than a solar gas but are still below the $f\text{O}_2$ of IW+1 (at 1700 K) found by Ihinger and Stolper (1986) for the lower limit of orange hibonite stability. Thus, if the orange color of the Allende hibonite were due to its condensation conditions, it should exhibit large, negative Ce anomalies, but none are observed. It is unlikely that Ce condensed into another phase and was later redistributed. This would require efficient diffusion into all phases, in just the right amounts needed to erase large anomalies. Because

FIG. 7. (below and right) $\delta^{26}\text{Mg}$ vs. $^{27}\text{Al}/^{24}\text{Mg}$, corrected for mass-fractionation, for the three hibonite-bearing inclusions. Assuming $\delta^{26}\text{Mg} = 0$ for $^{27}\text{Al}/^{24}\text{Mg} = 0$, all three inclusions have $\delta^{26}\text{Mg}$ consistent with $(^{26}\text{Al}/^{27}\text{Al})_i$ of 5×10^{-5} , as shown by the proximity of the data points to the reference line. There is no evidence that live ^{26}Al was present in the corundum in ALH2. The line for $(^{26}\text{Al}/^{27}\text{Al})_i = 0$ is shown for reference. Uncertainties are 1σ . (a) ALH1. (b) ALH2. (c) ALH3.





vaporization of oxides and silicates can produce locally oxidizing conditions (Davis *et al.*, 1982; Wang *et al.*, 1993, 2001; Floss *et al.*, 1996), hibonite formed as a volatilization residue of such material is expected to be orange but would also exhibit large negative Ce anomalies (Floss *et al.*, 1996). Hibonite that is strongly depleted in Ce and in V has been found in Allende (Davis *et al.*, 1982) and in Murchison (Ireland *et al.*, 1992), and these features have been attributed to distillation in the nebula (Ireland *et al.*, 1992). Because no scenario involving formation of ALH hibonite under oxidizing conditions is consistent with our Ce data, we conclude that the chondrite-normalized REE abundances provide further evidence for the initial formation of the ALH hibonite under reducing conditions.

Evidence from V Contents—The behavior of V also varies with oxygen fugacity, so it can provide some useful information. Under oxidizing conditions, V behaves like a volatile element and is not expected to be incorporated into hibonite condensed under such conditions. For example, Davis *et al.* (1982) calculated a solid/gas distribution coefficient for V in a CI gas at 1723 K (an oxygen fugacity approximately at IW, six orders of magnitude above that of a solar gas) that is one-thousandth of that in a solar gas at the same temperature. Also, V is readily lost from silicate melts in 1–2 days at an fO_2 of 10^{-14} (IW-3) at 1550 K (J. Beckett, unpubl. data). Orange hibonite is known to be stable only at much higher oxygen fugacities (IW+1). We would therefore not expect V to be present in hibonite formed at such relatively high oxygen fugacities, but the (orange) hibonite in the ALH samples is quite enriched in V_2O_3 relative to hibonite from Murchison. We cannot completely rule out the possibility that the hibonite was originally V_2O_3 -poor and that V was added later, but this seems unlikely. Probably the most common way that phases in refractory inclusions become secondarily enriched in V_2O_3 is by assimilation during or after oxidation of V-rich opaque assemblages. According to Blum *et al.* (1989), the opaque assemblages found in refractory inclusions originated as molten alloy droplets that were immiscible in host silicate liquids. At temperatures >1800 K and solar oxygen fugacities, metallic V would partition into these alloys. During cooling of CAIs, even in a solar gas, the V metal should oxidize, first to VO and then to V_2O_3 (Blum *et al.*, 1989). This apparently resulted in local enrichments in V_2O_3 in fassaite, magnetite and spinel in cases where these phases occur adjacent to opaque assemblages, but this effect has not been shown to occur in hibonite, and opaque assemblages have not been observed in the present samples. Also, the ubiquitous high V_2O_3 contents seen in hibonite and spinel in the ALH inclusions are unlike the local enrichments associated with opaque assemblages. We conclude that the high V contents of the hibonite in our samples are primary, and are not consistent with formation under conditions inferred for orange hibonite by Ihinger and Stolper (1986).

In summary, calculations show that Ce and V are quite volatile at IW (Davis *et al.*, 1982) and perhaps at oxygen

fugacities as low as IW-3 (Beckett *et al.*, 1988; J. Beckett, unpubl. data), but the ALH hibonite is not depleted in these elements. Therefore, the ALH hibonite probably originally formed at oxygen fugacities below IW-3. This would account for the lack of Ce and V depletions and the evidence for the original presence of Ti^{3+} . Calculations by Beckett *et al.* (1988) based on their experimental results show that this fugacity is sufficiently reducing for Ti^{3+} to be present in hibonite.

Formation of the Inclusions

In order to make some inferences regarding the origin of these inclusions, we must assess whether our data and observations are more consistent with an igneous, gas-to-solid condensation, or evaporative origin for these inclusions, or perhaps some combination of these processes.

Let us start by considering formation of the inclusions by crystallization of melts with the observed bulk compositions. Published phase equilibria (Stolper, 1982; Beckett and Stolper, 1994) show that for these compositions, spinel should crystallize first, then melilite, followed by grossite and hibonite in ALH1 and by monticellite in ALH2 and ALH3. There are several arguments against formation of the ALH inclusions by simple fractional crystallization. One is that the observed phase assemblages do not match those predicted by phase equilibria. Neither grossite nor monticellite are present in the inclusions although theoretically these phases should follow melilite. Hibonite is present; it could crystallize late in ALH1, after spinel, melilite, and grossite, but it is found enclosed in melilite. It should not crystallize at all from the ALH2 or ALH3 compositions, and many of the laths are rounded or corroded, indicating that it was not stable and probably is relic. Allen *et al.* (1978) also concluded that the phase assemblage observed in CG-11, whose composition is very similar to that of ALH1, was not consistent with crystallization from a melt.

The chondrite-normalized REE patterns of hibonite and melilite do not appear to be consistent with igneous partitioning, further suggesting that the hibonite is relic. Experiments have shown that hibonite/liquid distribution coefficients (D_s) decrease sharply from La (~ 6) through Lu (< 0.1) (Kennedy *et al.*, 1994). Although the LREE are strongly compatible in hibonite and incompatible in melilite (Kuehner *et al.*, 1989; Beckett *et al.*, 1990), the melilite in ALH1 has LREE contents that are higher than those of hibonite (Fig. 6). In both phases and in perovskite as well, in both ALH1 and ALH2, the REE abundances do not decrease from La through Lu as do the D_s . In light of the D_s , crystallization from a melt of hibonite and perovskite with flat or HREE-enriched patterns, would require either rapid crystallization, a strongly HREE-enriched bulk composition, or extensive prior crystallization of a LREE-enriched phase. The melilite is not dendritic, which argues against very fast cooling, and the generally flat REE patterns of melilite rule out a HREE-enriched bulk composition. We have not observed a LREE-enriched phase in these inclusions.

In ALH3, the REE patterns for the different phases probably reflect formation from the same volatility-fractionated (Group II) source. The flat LREE abundances, especially in melilite and perovskite, resemble the relative abundances predicted for solid/gas partitioning in a solar gas at 1723 K (Davis *et al.*, 1982), with no suggestion of an igneous overprint.

The textures also strongly suggest that the hibonite in these inclusions is relic. The hibonite, and the spinel intergrown with it, may have been present in the nebula as loose clumps of grains that became enclosed in a silicate vapor or liquid in which they were not stable and therefore began to evaporate or dissolve, forming the corroded grains and rafts of hibonite + spinel that we observe. Where hibonite and spinel were intergrown, the fluid that they were reacting with was sealed out and the straight hibonite/spinel contacts preserved. Thermodynamic calculations for $P^{\text{tot}} = 10^{-3}$ atm (Yoneda and Grossman, 1995) show that hibonite should begin to react with the nebular gas to form gehlenite at 1628 K and then spinel at 1500 K. The lath-shaped spinel in the ALH samples probably reflects pseudomorphic replacement of hibonite in the nebula, as was suggested for Murchison inclusion SH-6 (MacPherson *et al.*, 1984), an inclusion in which lath-shaped spinel forms a mantle around a core of euhedral hibonite plates. Individual laths that are part-hibonite and part-spinel occur at the core/mantle contact. The texture of SH-6 provides strong petrographic evidence that hibonite reacted with the nebular gas to form spinel, and the spinel replaced the hibonite pseudomorphically.

Isolated grains of spinel may be native to the ALH inclusions, but most of the spinel/melilite contacts are rounded, indicating that spinel, too, became unstable at some point. From the bulk compositions of the inclusions and the isotherms of the spinel saturation surface (Stolper, 1982), we estimate that temperatures in excess of 1800 K would be required to begin dissolving spinel in these inclusions. At such temperatures, the melilite would also melt and, under most nebular conditions, the melt would begin losing MgO and SiO₂ by evaporation. Upon cooling, crystallization during continued evaporation might account for the reverse zoning and Mg-isotopic fractionation observed in melilite. The isotopically heavy magnesium in all three ALH inclusions is consistent with this idea. $\Delta^{25}\text{Mg}$ values of 5 to 10‰ imply loss of 30 to 45% of the amount of magnesium initially present. According to calculations by Ebel and Grossman (2000b), slow cooling allows sufficient evaporative loss of Mg and Si to cause reverse zoning in melilite; faster cooling would lead to normally-zoned or unzoned grains. The specific cooling rate needed for a given zoning trend depends upon several parameters, including droplet size and composition, and total pressure.

Hibonite in all three inclusions also has isotopically heavy Mg. This probably reflects the composition of its source, because the absence of Ce anomalies shows that it has not been distilled, and its Mg-Al systematics have not been disturbed, which rules out isotopic exchange.

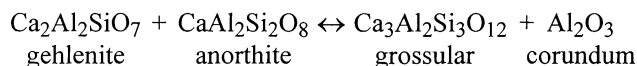
The ²⁶Al-²⁶Mg systematics of all three inclusions are consistent with hibonite formation with a ²⁶Al/²⁷Al ratio of 5×10^{-5} , the canonical early solar system ratio (MacPherson *et al.*, 1995). In all three ALH inclusions, melilite lies slightly below the ²⁶Al/²⁷Al = 5×10^{-5} isochron. The data are permissive of later crystallization of melilite or partial metamorphic resetting of melilite up to 1 Ma after hibonite crystallization.

Origin of Corundum and CaTs in These Inclusions

In addition to significant amounts of hibonite, ALH1 and ALH2 contain subhedral corundum grains. There are several lines of evidence that suggest that the grains are secondary alteration products rather than primary phases. First, thermodynamic calculations (Yoneda and Grossman, 1995; Ebel and Grossman, 2000a) show that during equilibrium condensation, corundum should react with the solar nebular gas to form hibonite. Thus, if the corundum in these samples is a primary high-temperature condensate, we would expect it to be enclosed in or commonly in contact with hibonite, but we found only one such occurrence. Second, if the corundum is a primary or relic phase, it is difficult to envision how it could have avoided becoming rounded or corroded like much of the hibonite and spinel in these inclusions; yet the corundum grains have straight, fresh-looking crystal faces and do not appear to have been in the process of reacting. Third, all of the corundum grains are partially to completely enclosed in grossular \pm nepheline, common secondary alteration products. Finally, many ion probe analyses (Fig. 7) show that melilite, hibonite and spinel contain excess ²⁶Mg abundances that are consistent with *in situ* decay of ²⁶Al and $(^{26}\text{Al}/^{27}\text{Al})_{\text{I}} = 5 \times 10^{-5}$, and melilite was either disturbed or crystallized with $(^{26}\text{Al}/^{27}\text{Al})_{\text{I}} = (2-3) \times 10^{-5}$, but the isotopic composition of corundum in ALH2 implies far lower initial ²⁶Al/²⁷Al ratios. This indicates that the corundum in this sample either formed prior to injection of live ²⁶Al into the nebula, well before the other phases in the inclusions formed, or several million years after the other phases formed, after ²⁶Al had decayed. Early formation seems unlikely, as it would probably require the grains to experience a lengthy nebular history in hostile environments, yet survive virtually uncorroded. It is also quite unlikely that the corundum had the canonical $(^{26}\text{Al}/^{27}\text{Al})_{\text{I}}$ and had its isotopic systematics severely disturbed while those of hibonite and spinel were not. Corundum with very small ²⁶Mg excesses was also found in an inclusion from Murchison (Bar-Matthews *et al.*, 1982), but that isotopic composition is thought to be representative of the source of the inclusion, because it is the same as that of the hibonite in that inclusion.

Alternatively, instead of being primary, the ALH corundum grains could have formed during alteration of the CAIs. Such an origin would be consistent with the apparent freshness of the grains, their association with grossular and nepheline, and their low excess ²⁶Mg. Alteration products in some Type B inclusions from Allende also typically lack excess ²⁶Mg,

indicating that alteration of the inclusions occurred at least ~2.4 Ma after crystallization of the primary phases (Davis *et al.*, 1994). Alteration of melilite commonly gives rise to assemblages rich in grossular + monticellite, the latter phase forming from the åkermanite component of the melilite. Corundum is rare as an alteration product, but may occur here instead of monticellite because of the comparatively aluminous compositions of the melilite that was altered to form the secondary minerals. Secondary anorthite is present in the inclusions, and it could have locally reacted with adjacent melilite to form corundum *via* the reaction



This assemblage is in equilibrium at 1000 K and one bar pressure, with gehlenite + anorthite stable at higher temperatures and grossular + corundum stable at lower temperatures. If this reaction took place, it would imply that the corundum-bearing inclusions experienced slow cooling through 1000 K. It has previously been suggested, based on studies of opaque assemblages in CAIs, chondrules, and matrix (Blum *et al.*, 1989), that Allende CAIs experienced cooling rates on the order of 10^{-6} K per hour through 770 K, along a NiFe alloy-oxide buffer at an oxygen fugacity six orders of magnitude above that of a solar gas. Extrapolating this T - $f\text{O}_2$ path to higher temperatures, at 1000 K, where the corundum might have formed, the oxygen fugacity would have been about seven log units greater than that of a solar gas. Perhaps such conditions are sufficiently oxidizing and hot for the blue-to-orange transition to occur in hibonite. The experiments of Ihinger and Stolper (1986) were all at 1700 K, and they showed that the transition occurs at an $f\text{O}_2$ seven log units above solar at that temperature.

The discovery of CaTs in ALH1 is quite unexpected and somewhat puzzling, as there is no known stability field for this phase at or below atmospheric pressures. It is probably a metastable breakdown product of Al-rich melilite, occurring here, as in the case of corundum, due to the Mg-poor composition of the primary melilite. Metastable phases usually require rapid cooling in order to be preserved, however, which conflicts with the slow cooling and equilibration implied above. Perhaps the CaTs formed at higher temperatures than the corundum did, during relatively rapid cooling, which was followed by relatively slow cooling through temperatures that were high enough for corundum to form, but low enough to allow preservation of the CaTs grains.

Thermal Histories and the Color of Hibonite

In contrast to Allende, CM2 chondrites contain Fe-rich phyllosilicates, indicating that these meteorites must have been exposed to very oxidizing conditions. Yet blue hibonite is preserved in their CAIs, which suggests that in addition to

relatively high oxygen fugacities, elevated temperatures are required for the blue-to-orange transition in hibonite. Phyllosilicates are also present in the matrix of the Vigarano CV3 chondrite (Lee *et al.*, 1996), a member of the reduced subgroup (McSween, 1977) of CV chondrites that contains CAIs with blue hibonite. The temperature (~1000 K) inferred above for corundum formation and possible hibonite oxidation is well above the maximum temperatures suggested for alteration of CM (~320 K) and CV (~420 K) matrices (Zolensky *et al.*, 1993). After accretion, the CMs and Vigarano must have remained below the blue-to-orange transition temperatures for the oxygen fugacities that they experienced. It would be interesting to study hibonite from chondrites with different thermal histories to see if there is any correlation between hibonite color and the inferred conditions of alteration (maximum temperature, $f\text{O}_2$, water/rock ratio). Finally, a series of experiments on the blue-to-orange transition in hibonite, run at lower temperatures than those of Ihinger and Stolper (1986), would better constrain the conditions under which this transition occurs and would place valuable constraints on the thermal histories of CM2 and CV3 chondrites.

CONCLUSIONS

Hibonite found in refractory inclusions in CM2 chondrites is blue, while that in Allende is orange. Studies have shown that blue hibonite contains Ti^{3+} while orange hibonite does not (Ihinger and Stolper, 1986; Beckett *et al.*, 1988). Ihinger and Stolper (1986) favored formation of orange hibonite by oxidation of Ti^{3+} -bearing hibonite rather than by condensation in the nebula under extremely oxidizing conditions. Our study is the first to test this idea through detailed analysis of Allende hibonite. Our results, which show that there are slight excesses of Ti + Si relative to Mg + Fe, high V_2O_3 contents and no Ce anomalies in Allende hibonite, support their suggestion. Hibonite in the samples we studied formed under reducing conditions, probably within 2–3 orders of magnitude of the $f\text{O}_2$ of a solar gas; at higher oxygen fugacities, V and Ce depletions would occur (Davis *et al.*, 1982). Because all of the experiments of Ihinger and Stolper were conducted at one temperature, 1700 K, additional experiments are needed to better constrain the blue-to-orange transition conditions. Such work would improve our understanding of the thermal histories of refractory inclusions and of the parent bodies of their hosts.

The samples considered here did not simply crystallize from melts of the observed bulk compositions. The hibonite and perhaps some of the spinel in them is relic. These phases became unstable at some point, perhaps due to heating and melting. The reversely zoned melilite may reflect simultaneous crystallization and evaporative loss of MgO and SiO_2 during a heating event. Alteration of the gehlenitic melilite in these samples gave rise to unusual, Mg-poor secondary alteration products which include corundum and CaTs.

Acknowledgements—Reviews by C. Floss and S. Russell led to improvements in the text. This work was supported by the National Aeronautics and Space Administration (NASA) through grants NAG5-4476 (L. G.) and NAG5-4928 and NAG5-9510 (A. M. D.), and funding is gratefully acknowledged.

Editorial handling: D. W. Mittlefehldt

REFERENCES

- ALLEN J. M., GROSSMAN L., DAVIS A. M. AND HUTCHEON I. D. (1978) Mineralogy, textures and mode of formation of a hibonite-bearing Allende inclusion. *Proc. Lunar Planet. Sci. Conf.* **9th**, 1209–1233.
- BAR-MATTHEWS M., HUTCHEON I. D., MACPHERSON G. J. AND GROSSMAN L. (1982) A corundum-rich inclusion in the Murchison meteorite. *Geochim. Cosmochim. Acta* **46**, 31–41.
- BECKETT J. R. (1986) The origin of calcium-, aluminum-rich inclusions from carbonaceous chondrites: An experimental study. Ph.D. thesis, University of Chicago, Chicago, Illinois, USA. 373 pp.
- BECKETT J. R. AND STOLPER E. M. (1994) The stability of hibonite, melilite and other aluminous phases in silicate melts: Implications for the origin of hibonite-bearing inclusions from carbonaceous chondrites. *Meteoritics* **29**, 41–65.
- BECKETT J. R., LIVE D., TSAY F.-D., GROSSMAN L. AND STOLPER E. (1988) Ti^{3+} in meteoritic and synthetic hibonite. *Geochim. Cosmochim. Acta* **52**, 1479–1495.
- BECKETT J. R., SPIVACK A. J., HUTCHEON I. D., WASSERBURG G. J. AND STOLPER E. M. (1990) Crystal chemical effects on the partitioning of trace elements between mineral and melt: An experimental study of melilite with applications to refractory inclusions from carbonaceous chondrites. *Geochim. Cosmochim. Acta* **54**, 1755–1774.
- BLUM J. D., WASSERBURG G. J., HUTCHEON I. D., BECKETT J. R. AND STOLPER E. M. (1989) Origin of opaque assemblages in C3V meteorites: Implications for nebular and planetary processes. *Geochim. Cosmochim. Acta* **53**, 543–556.
- BREARLEY A. J. AND JONES R. H. (1998) Chondritic meteorites. In *Planetary Materials* (ed. J. J. Papike), pp. 3-1 to 3-398. Reviews in Mineralogy **36**, Mineralogical Society of America, Washington, D.C., USA.
- CLAYTON R. N., HINTON R. W. AND DAVIS A. M. (1988) Isotopic variations in the rock-forming elements in meteorites. *Phil. Trans. Royal Soc. Lond.* **A325**, 483–501.
- DAVIS A. M., TANAKA T., GROSSMAN L., LEE T. AND WASSERBURG G. J. (1982) Chemical composition of HAL, an isotopically-unusual Allende inclusion. *Geochim. Cosmochim. Acta* **46**, 1627–1651.
- DAVIS A. M., SIMON S. B. AND GROSSMAN L. (1994) Alteration of Allende Type B1 CAIs: When, where and how (abstract). *Lunar Planet. Sci.* **25**, 315–316.
- EBEL D. S. AND GROSSMAN L. (2000a) Condensation in dust-enriched systems. *Geochim. Cosmochim. Acta* **64**, 339–366.
- EBEL D. S. AND GROSSMAN L. (2000b) Melilite zoning during partial evaporation of calcium-aluminum-rich inclusion droplets (abstract). *Meteorit. Planet. Sci.* **35** (Suppl.), A49–A50.
- FLOSS C., EL GORESY A., ZINNER E., KRANSEL G., RAMMENSEE W. AND PALME H. (1996) Elemental and isotopic fractionations produced through evaporation of the Allende CV chondrite: Implications for the origin of HAL-type hibonite inclusions. *Geochim. Cosmochim. Acta* **60**, 1975–1997.
- FUCHS L. H. (1971) Occurrence of wollastonite, rhönite, and andradite in the Allende meteorite. *Am. Mineral.* **56**, 2053–2068.
- GROSSMAN L. (1972) Condensation in the primitive solar nebula. *Geochim. Cosmochim. Acta* **36**, 597–619.
- GROSSMAN L. (1980) Refractory inclusions in the Allende meteorite. *Ann. Rev. Earth Planet. Sci.* **8**, 559–608.
- GROSSMAN L., EBEL D. S., SIMON S. B., DAVIS A. M., RICHTER F. M. AND PARSAD N. M. (2000) Major element chemical and isotopic compositions of refractory inclusions in C3 chondrites: The separate roles of condensation and evaporation. *Geochim. Cosmochim. Acta* **64**, 2879–2894.
- IHINGER P. D. AND STOLPER E. (1986) The color of meteoritic hibonite: An indicator of oxygen fugacity. *Earth Planet. Sci. Lett.* **78**, 67–79.
- IRELAND T. R., FAHEY A. J. AND ZINNER E. K. (1988) Trace-element abundances in hibonites from the Murchison carbonaceous chondrite: Constraints on high-temperature processes in the solar nebula. *Geochim. Cosmochim. Acta* **52**, 2841–2854.
- IRELAND T. R., FAHEY A. J. AND ZINNER E. K. (1991) Hibonite-bearing microspherules: A new type of refractory inclusions with large isotopic anomalies. *Geochim. Cosmochim. Acta* **55**, 367–379.
- IRELAND T. R., ZINNER E. K., FAHEY A. J. AND ESAT T. M. (1992) Evidence for distillation in the formation of HAL and related hibonite inclusions. *Geochim. Cosmochim. Acta* **56**, 2503–2520.
- KENNEDY A. K., LOFGREN G. E. AND WASSERBURG G. J. (1994) Trace-element partition coefficients for perovskite and hibonite in meteorite compositions. *Chem. Geol.* **117**, 379–390.
- KUEHNER S. M., LAUGHLIN J. R., GROSSMAN L., JOHNSON M. L. AND BURNETT D. S. (1989) Determination of trace element mineral/liquid partition coefficients in melilite and diopside by ion and electron probe techniques. *Geochim. Cosmochim. Acta* **53**, 3115–3130.
- LEE M. R., HUTCHISON R. AND GRAHAM A. L. (1996) Aqueous alteration in the matrix of the Vigarano (CV3) carbonaceous chondrite. *Meteorit. Planet. Sci.* **31**, 477–483.
- MACPHERSON G. J. AND DAVIS A. M. (1993) A petrologic and ion microprobe study of a Vigarano Type B refractory inclusion: Evolution by multiple stages of alteration and melting. *Geochim. Cosmochim. Acta* **57**, 231–243.
- MACPHERSON G. J. AND DAVIS A. M. (1994) Refractory inclusions in the prototypical CM chondrite, Mighei. *Geochim. Cosmochim. Acta* **58**, 5599–5625.
- MACPHERSON G. J. AND GROSSMAN L. (1984) "Fluffy" Type A Ca-, Al-rich inclusions in the Allende meteorite. *Geochim. Cosmochim. Acta* **48**, 29–46.
- MACPHERSON G. J., BAR-MATTHEWS M., TANAKA T., OLSEN E. AND GROSSMAN L. (1983) Refractory inclusions in the Murchison meteorite. *Geochim. Cosmochim. Acta* **47**, 823–839.
- MACPHERSON G. J., GROSSMAN L., HASHIMOTO A., BAR-MATTHEWS M. AND TANAKA T. (1984) Petrographic studies of refractory inclusions from the Murchison meteorite. *Proc. Lunar Planet. Sci. Conf.* **15th**, *J. Geophys. Res.* **89** (Suppl.), C299–C312.
- MACPHERSON G. J., DAVIS A. M. AND ZINNER E. K. (1995) The distribution of aluminum-26 in the early solar system—A reappraisal. *Meteoritics* **30**, 365–386.
- MCSWEN H. Y., JR. (1977) Petrographic variations among carbonaceous chondrites of the Vigarano type. *Geochim. Cosmochim. Acta* **41**, 1777–1790.
- NAZAROV M. A., PATCHEN A. AND TAYLOR L. A. (2000) Rhonite-bearing Ca-Al-rich inclusions of the Efremovka (CV3) chondrite (abstract). *Lunar Planet. Sci.* **31**, #1242, Lunar and Planetary Institute, Houston, Texas, USA (CD-ROM).
- POUCHOU J. L. AND PICOIR F. (1984) A new model for quantitative X-ray microanalysis. Part I: Application to the analysis of homogeneous samples. *Rech. Aerosp.* **1984-3**, 13–38.
- RUSSELL S. S., DAVIS A. M., MACPHERSON G. J., GUAN Y. AND HUSS G. R. (2000) Refractory inclusions from the ungrouped carbonaceous chondrites MAC 87300 and MAC 88107. *Meteorit. Planet. Sci.* **35**, 1051–1066.

- SIMON S. B., GROSSMAN L. AND DAVIS A. M. (1991) Fassaite composition trends during crystallization of Allende Type B refractory inclusion melts. *Geochim. Cosmochim. Acta* **55**, 2635–2655.
- SIMON S. B., GROSSMAN L. AND DAVIS A. M. (1997) Multiple generations of hibonite in spinel-hibonite inclusions from Murchison. *Meteorit. Planet. Sci.* **32**, 259–269.
- SIMON S. B., DAVIS A. M. AND GROSSMAN L. (1998a) Hibonite in Allende and Murchison refractory inclusions and implications of the absence of cerium depletions (abstract). *Meteorit. Planet. Sci.* **33 (Suppl.)**, A145–146.
- SIMON S. B., DAVIS A. M., GROSSMAN L. AND ZINNER E. K. (1998b) Origin of hibonite-pyroxene spherules found in carbonaceous chondrites. *Meteorit. Planet. Sci.* **33**, 411–424.
- SIMON S. B., DAVIS A. M. AND GROSSMAN L. (1999) Origin of compact Type A refractory inclusions from CV3 carbonaceous chondrites. *Geochim. Cosmochim. Acta* **63**, 1233–1248.
- STOLPER E. M. (1982) Crystallization sequences of Ca-Al-rich inclusions from Allende: An experimental study. *Geochim. Cosmochim. Acta* **46**, 2159–2180.
- WANG J., DAVIS A. M. AND CLAYTON R. N. (1993) Rare earth element fractionation during evaporation of chondritic material (abstract). *Meteoritics* **28**, 454–455.
- WANG J., DAVIS A. M., CLAYTON R. N., MAYEDA T. K. AND HASHIMOTO A. (2001) Chemical and isotopic fractionation during the evaporation of the FeO-MgO-SiO₂-CaO-Al₂O₃-TiO₂-REE melt system. *Geochim. Cosmochim. Acta*, in press.
- WARK D. A. (1986) Evidence for successive episodes of condensation at high temperature in a part of the solar nebula. *Earth Planet. Sci. Lett.* **77**, 129–148.
- WARK D. A. AND LOVERING J. F. (1977) Marker events in the early evolution of the solar system: Evidence from rims on Ca-Al-rich inclusions in carbonaceous chondrites. *Proc. Lunar Sci. Conf.* **8th**, 95–112.
- YONEDA S. AND GROSSMAN L. (1995) Condensation of CaO-MgO-Al₂O₃-SiO₂ liquids from cosmic gases. *Geochim. Cosmochim. Acta* **59**, 3413–3444.
- ZOLENSKY M., BARRETT R. AND BROWNING L. (1993) Mineralogy and composition of matrix and chondrule rims in carbonaceous chondrites. *Geochim. Cosmochim. Acta* **57**, 3123–3148.